Complete framework of wind-vehicle-bridge interaction with random road surfaces

A. Camara[1], I. Kavrakov[2], K. Nguyen[3], G. Morgenthal[2]

1: Department of Civil Engineering. City, University of London. Northampton Square, London, EC1V 0HB, United Kingdom

2: Chair of Modelling and Simulation of Structures, Bauhaus University Weimar, 99423 Weimar, Germany

3: Escuela Técnica Superior De Ingeniería Aeronáutica y del Espacio, Universidad Politécnica de Madrid, Pza. Cardenal Cisneros, 28040, Madrid, Spain

Abstract

The risk of vehicle accidents and discomfort under wind actions is key in the serviceability assessment of long-span bridges. This paper presents a complete wind-vehicle-bridge interaction (W-VBI) framework in which the pavement irregularities are simulated as random surfaces that include the bridge joints instead of traditional one-dimensional (1D) road profiles. The methodology includes a new approach to assess the safety and comfort of all the users of the bridge, including those in the vehicles and on the deck, and to account for the variability of the response. The application of the proposed W-VBI framework in the study of a long cable-stayed bridge demonstrated that the driving safety and the pedestrians' comfort cannot be based on the analysis of a single record, and guidance is proposed to obtain results with statistical significance. Moreover, it is observed for the first time that 1D road irregularity models can significantly underpredict the risk of discomfort and of driving instabilities in bridges subjected to crosswinds. Finally, the direct connection between the quality of the road and the comfort in the vehicles is clearly established, which has potential implications on pavement monitoring programmes.

Keywords:
Long-span bridges; wind-vehicle-bridge interaction; road surface; pavement

Email address: `alfredo.camara@city.ac.uk` (A. Camara[1])

conditions; driving safety; comfort.

Nomenclature

α_s	Angle between the wind and the deck section in static equilibrium
$\bar{\eta}^*$	Bootstrap replication of the mean performance ratio
$\bar{\eta}^V$	Mean performance ratio for the driving speed V
$\bar{\eta}^{*(2.5\%)}; \bar{\eta}^{*(97.5\%)}$	2.5^{th} and the 97.5^{th} percentile of the bootstrap distribution
$\bar{r}_L; \bar{r}_W$	Filtered leeward and windward pavement irregularity profiles
$\boldsymbol{\eta}$	Vector with the performance ratios η obtained in the analysis
$\boldsymbol{\eta}^*$	Vector containing the bootstrap sample of $\boldsymbol{\eta}$
$\boldsymbol{f}_{b,w-b}$	Buffeting wind force vector in the bridge
$\boldsymbol{f}_{b,w-se}$	Aeroelastic wind force vector in the bridge
$\boldsymbol{f}_{b,w-s}$	Mean wind force vector in the bridge
χ	Aerodynamic admittance functions of the deck
Δn	Frequency resolution in the pavement generation
Δr	Spacing between consecutive points in the pavement profile
$\eta_{a,G}$	Global (overall) accident ratio
$\eta_{a,o}$	Overturning accident ratio
$\eta_{a,s}$	Side-slip accident ratio
$\eta_{c,b-j}$	Pedestrians' discomfort ratio in the direction $j = Y, Z$
$\eta_{c,v}$	Vehicle users' discomfort ratio
$\boldsymbol{\Phi}$	Vibration mode shape matrix of the structure
$\mathbf{C}_b^v$	Contribution of the vehicles to the bridge damping matrix

2

$\mathbf{C}_i$	Damping matrix of the bridge ($i = b$) or the vehicle ($i = v$)
$\mathbf{C}_{v,b}; \mathbf{C}_{b,v}$	Coupling vehicle/bridge damping matrices
$\mathbf{f}_{i,r}$	Force vector due to the wheel-pavement contact in the bridge ($i = b$) or in the vehicle ($i = v$)
$\mathbf{f}_{i,w}$	Force vector due to the wind in the bridge ($i = b$) or in the vehicle ($i = v$)
$\mathbf{f}_{v,g}$	Force vector due to gravity on the vehicles
$\mathbf{K}_b^v$	Contribution of the vehicles to the bridge stiffness matrix
$\mathbf{K}_i$	Stiffness matrix of the bridge ($i = b$) or the vehicle ($i = v$)
$\mathbf{K}_{v,b}; \mathbf{K}_{b,v}$	Coupling vehicle/bridge stiffness matrices
$\mathbf{M}_i$	Mass matrix of the bridge ($i = b$) or the vehicle ($i = v$)
$\mathbf{q}_i$	Displacement vector of the bridge ($i = b$) or the vehicle ($i = v$)
μ_c	Tyre-pavement friction coefficient
ω	Circular frequency of the bridge motion
ψ	Instantaneous angle of incidence of the wind on the vehicles
ρ	Density of the air
σ	Standard deviation
$\theta_k; \phi_k$	Random phase angles in the pavement generation
ξ	Modal damping ratio of the structure
A_v	Reference surface of the vehicle
$a_{\mathrm{adm}-b,j}$	Admissible acceleration in the deck in the direction $j = Y, Z$
$a_{\mathrm{adm}-v}$	Admissible acceleration in the vehicle
$a_{\mathrm{RMS}-v,j}$	RMS acceleration at the driver's seat in the $j = Y, Z$ direction

$a_{i,j}$	Acceleration of the deck ($i = b$) or the vehicle ($i = v$) in the $j = Y, Z$ direction
$a_{w-v,j}$	Weighted acceleration at the driver's seat in the $j = Y, Z$ direction
a_{w-v}	Weighted acceleration at the driver's seat, combined from the $j = Y, Z$ directions
B	Width of the deck
b	Half-distance between wheel lines in the transverse direction
b_d	Transverse distance between the driver's seat and the centroid of the vehicle
B_r	Order of the bootstrap replication
$C^i; C^j$	Static aerodynamic coefficients of the vehicle
$C_D; C_L; C_M$	Drag, lift and moment static coefficients of the deck
$C'_D; C'_L; C'_M$	Derivatives of the drag, lift and moment static coefficients of the deck with respect to the angle of attack
d	Along-drive distance between the contact point and the center of the corresponding wheel
$f^i_{v,w}$	Individual components of the wind force on the vehicle
$f^S_{v,w}$	Side wind force on the vehicle (Y direction)
$f_l; f_c; f_u$	Lower, central and upper frequencies of each octave band of $S_{a_{i,j}a_{i,j}}$
$F_{c,i-j}$	Pavement contact force of the wheel $j = 1, \cdots, 4$ in the direction $i = Y, Z$
$F_{c,i-L}; F_{c,i-W}$	Sum of the pavement contact forces in the leeward or the windward wheels in the direction $i = Y, Z$
G_d	Target one-sided PSD of displacements in the pavement generation

$G_{d,x}$ One-sided cross PSD function in the pavement generation

h_v Distance between the vehicle centroid and the centroid of the deck

I_n turbulence intensity in n-direction, with $n = u, v, w$

K Reduced frequency

L_c Longitudinal distance between the vehicle cabin and its centroid

N Number of discrete spatial frequencies in the pavement generation

n_0 Discontinuity frequency in the pavement generation

n_1, n_N Lower and upper cut-off spatial frequencies in the pavement generation

N_r Number of independent pavement and wind records

$p; h; \alpha$ Lateral, vertical and rotational movement of the 3 DOF deck sectional model

$P^*; H^*; A^*$ Flutter derivatives of the deck section

R Autocorrelation function of the pavement irregularity surface

$r_L; r_W$ Leeward and windward pavement irregularity profiles

R_W Wheel radius

$S_{a_{i,j} a_{i,j}}$ PSD of $a_{i,j}$

$t_O; t_S$ Time instants of high risk of vehicle overturning or side-slipping

$t_{A1}; t_{T1}; t_{T2}; t_{T3}; t_{A2}$ Time instants in which the centroid of the 9-th vehicle passes the left abutment, the three towers, or the right abutment

U Mean wind speed

$u; v; w$	Instantaneous wind velocity in the along-flow, along-deck and vertical direction
$u_t; v_t; w_t$	Turbulence in the along-flow, along-deck and vertical direction
V	Vehicle driving speed
V_C	Critical driving speed beyond which accidents or discomfort occur
V_r	Resultant wind velocity acting on the vehicles
w_k	Weighting factor for the k-th octave band in the calculation of $a_{w-v,j}$
$W_{95}; \hat{W}_{95}$	Width and normalised width of the 95%-confidence interval of the mean performance ratio
x	Along-drive spatial coordinate
x_P	Longitudinal position of the wheel contact point
y	Across-drive spatial coordinate
z	Vertical spatial coordinate

1. Introduction

Long-span bridges are usually exposed to strong winds and have slender decks that are prone to vibrations. The operation of these structures under relatively low wind speeds is governed by the driving safety and the comfort of vehicle users or pedestrians.

The assessment of the driving safety involves the study of the critical wind velocities for which accidents may occur. In long-span bridges this entails a complex wind-vehicle-bridge interaction (W-VBI) problem that can only be captured if the coupling between the dynamic response of the bridge and the movement of the vehicle through the pavement irregularities is adequately considered. Previous works developed semi-analytical models that define the direct wind actions on the bridge and on the vehicles from their aerodynamic coefficients, and solve the equations of motion for the deck, the vehicle and their interaction under wind loading at every time-step [1, 2]. Since then, several researchers defined the coupled motion of the vehicles and the bridge. For computational efficiency, the latter is usually obtained as a linear superposition of the dynamic responses of uncoupled single degree-of-freedom (DOF) systems, see e.g. [3].

Most of the works on W-VBI are focused on the driving safety under stormy winds, but very few of them consider the users' comfort under the combination of relatively frequent wind velocities and traffic combinations. Xu and Guo [4] observed that the crosswind in the vehicle governs its lateral vibrations, whereas the bridge motion dominates the vertical vehicle vibrations when the pavement is very good. However, they noticed that large road irregularities are the main factor contributing to the vertical accelerations in the vehicles. This was echoed by Kavrakov *et al.* [5], who also concluded that the aerodynamic model of choice to define the wind forces on the deck is not essential for the assessment of the comfort to vertical vibrations in the vehicles. In a study based on the direct integration of the system of dynamics and the quasi-steady definition of the wind action, Nguyen *et al.* [6] observed the potential discomfort and fatigue of the drivers crossing a slender arch bridge due to the lateral vibrations induced by the crosswind. That work also studied the discomfort of pedestrians at a particular point of the deck (midspan). However, the pedestrians' comfort should be assessed in the entire length of the sidewalks to obtain a complete view of the problem.

The comfort and the driving safety are significantly affected by the irregularities of the pavement, which is an essential aspect in the vehicle-bridge

7

interaction [4, 6, 7, 8, 9]. The pavement irregularity profiles in W-VBI studies are usually generated by means of one-dimensional (1D) zero-mean stationary Gaussian random processes based on a Power Spectral Density (PSD) function defined by the normative ISO 8606 [10] or measured experimentally [11]. 1D road profiles consider the correlation between the irregularities in the longitudinal (along-drive) direction, but not in the transverse one. Following this approach, Chen and Cai [3] applied the same road irregularity profiles at the two wheel lines of the vehicles, which is known to overestimate the vehicle response in the absence of wind [12]. Most of the works on W-VBI do not report the type of transverse correlation that is considered between the road profiles at the two wheel lines [4, 13, 14].

As in the case of the pavement irregularities, the wind speed time-histories are also simulated as particular realisations of a random process that is generated from target spectra. Therefore, it is important to include sufficient samples of the pavement and the wind histories in order to obtain results with statistical meaning. Xu and Guo [2, 7] considered the average of five pavement records, whereas other works employed eight [5]. Unfortunately, most of the W-VBI studies do not report the number of records considered in the analysis, even though the driving safety and comfort are strongly influenced by the record-to-record variability, as it is observed in this research.

This work contributes with new knowledge on the vibration induced by spatially correlated pavement and wind records, which are important for the comfort and the driving safety in long-span bridges. This is achieved by developing a complete W-VBI framework with the following innovative aspects:

- the pavement irregularity surfaces applied at the wheel-deck contacts account for: (1) the filtering effects of the tyres, and (2) the bridge joints,

- the study of the driving accident risks and the potential discomfort of different types of users is based on critical wind curves that include statistical information about the variability of the results.

The application of the proposed W-VBI framework in a comprehensive study of a long cable-supported bridge shows the importance of the record-to-record variability in the pavement and in the wind, as well as their interaction. A minimum of 10 records is recommended for the safety and the comfort assessment of vehicles crossing long-span bridges, but the accurate study of the

pedestrians' comfort would require 100 or more different records. The large influence on the vehicle stability and comfort of the transverse correlation between the pavement profiles and of the road quality is also demonstrated. These results are important in the serviceability assessment and the operation of bridges.

2. Wind-vehicle-bridge interaction with pavement surfaces

The W-VBI framework proposed in this work is composed of 3 stages described in Fig. 1. The main novelties correspond to Stages 1 and 3, which are highlighted.

Stage 1: Definition of the bridge and the vibration sources

This stage corresponds to the *pre-processing* of the W-VBI problem and it involves the characterisation of the sources of vibration in the deck and in the vehicles, namely the wind, the traffic conditions and the pavement irregularities, as well as the dynamic properties of the bridge. The later is defined by means of the matrix containing the relevant vibration mode shapes ($\boldsymbol{\Phi}$) and the corresponding vibration frequencies from a finite element (FE) analysis of the structure, as shown in Fig. 1(a).
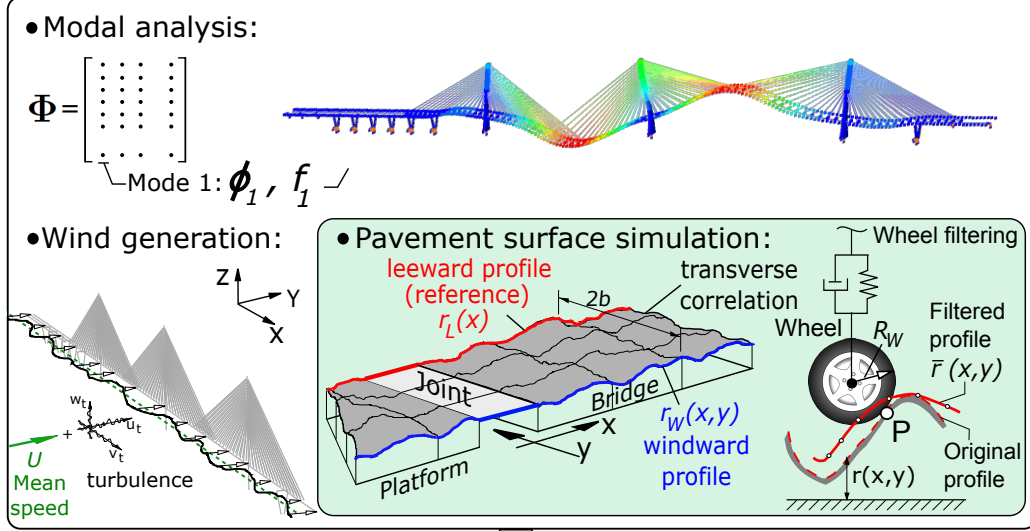
The wind speed time-histories at different points along the deck are generated from the mean wind speed and the turbulence properties. The simulation routines defined in [15] are employed to generate three-directional spatially correlated pseudo-random wind time-histories with prescribed PSD:

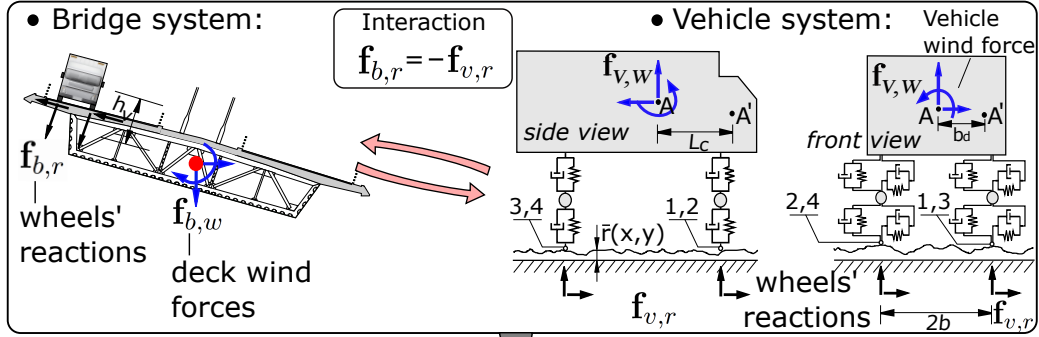$$u = U + u_t(x,t), \quad v = v_t(x,t), \quad w = w_t(x,t), \tag{1}$$

where u is the along-flow component of the wind speed (direction Y in Fig. 1(a)), which is decomposed into the mean wind speed (U) and the along-flow turbulence component (u_t); $v = v_t$ is the wind speed parallel to the direction of the deck (X); $w = w_t$ is the wind speed in the vertical direction (Z), as shown in Fig. 1(a). All the turbulent components (u_t, v_t, w_t) have zero-mean and their standard deviation (σ_n) is given by the site-specific turbulence intensity in the corresponding direction: $I_n = \sigma_n/U$, with $n = u, v, w$ referring to the wind component.

The traffic conditions need to be defined in order to position the vehicles in the deck during the analysis. This work assumes that the drivers' behaviour is not conditioned by the wind or by the movement of the bridge, which

9

(a) **Stage 1:** *Bridge and environment definition*

- Modal analysis:

$$\mathbf{\Phi} = \begin{bmatrix} \vdots & \vdots & \vdots & \vdots & \vdots \\ \cdot & \cdot & \cdot & \cdot & \cdot \\ \cdot & \cdot & \cdot & \cdot & \cdot \\ \vdots & \vdots & \vdots & \vdots & \vdots \end{bmatrix}$$

Mode 1: $\boldsymbol{\phi}_1$, f_1

- Wind generation:

z, Y, X

w_t u_t v_t

U Mean speed   turbulence

- Pavement surface simulation:

Wheel filtering

leeward profile (reference) $r_L(x)$ transverse correlation $2b$

Joint   Bridge   Wheel R_W Filtered profile $\bar{r}(x,y)$

$r_W(x,y)$ windward profile

Platform y x P   Original profile

$r(x,y)$

(b) **Stage 2:** *Dynamic analysis (repeat for each pavement and wind record)*

- Bridge system:

Interaction
$\mathbf{f}_{b,r} = -\mathbf{f}_{v,r}$

- Vehicle system: Vehicle wind force

h_v

$\mathbf{f}_{b,r}$

wheels' reactions

$\mathbf{f}_{b,w}$

deck wind forces

$\mathbf{f}_{v,w}$ A   A'   *side view* L_c

3,4   1,2 $\bar{r}(x,y)$

$\mathbf{f}_{v,r}$

$\mathbf{f}_{v,w}$ A   A'   *front view* b_d

2,4   1,3

wheels' reactions $2b$ $\mathbf{f}_{v,r}$

(c) **Stage 3:** *Safety and comfort assessment*

• Driving safety	• Vehicle comfort	• Pedestrians' comfort
overturn $\mathbf{f}_{v,r\text{-}Z} \longrightarrow \eta_{a,o} \pm \sigma$	Seat acceleration	Acceleration in the whole deck
$\begin{matrix} \mathbf{f}_{v,r\text{-}Z} \\ \mathbf{f}_{v,r\text{-}Y} \\ \mu_c \end{matrix} \begin{matrix} \text{side-slip} \\ \longrightarrow \eta_{a,s} \pm \sigma \end{matrix}$	$\begin{matrix} a_{v,Z} \\ a_{v,Y} \end{matrix} \longrightarrow \eta_{c,v} \pm \sigma$	$a_{b,Z} \longrightarrow \eta_{c,b\text{-}Z} \pm \sigma$ $a_{b,Y} \longrightarrow \eta_{c,b\text{-}Y} \pm \sigma$

Figure 1: Proposed W-VBI framework: (a) pre-processing, (b) analysis, (c) post-processing. The main novelties of this paper are highlighted in shaded boxes.

allows to position every vehicle at every instant before the W-VBI analysis is conducted. Additionally, the traffic is simplified as a convoy of equally spaced vehicles crossing the bridge at a constant velocity V in a straight path, occupying a single lane. These assumptions reduce the computational cost and are deemed acceptable to study the influence of the pavement and the wind randomness on the W-VBI problem, which is the scope of this paper. It should be noted that more realistic stochastic traffic flows such as those considered in [14] can be directly incorporated in the proposed W-VBI framework.

Following [6, 16] the pavement irregularities are defined as series of parallel longitudinal profiles that are correlated in the transverse direction (y, perpendicular to the traffic), as shown in Fig. 1(a). The wheel profile in the leeward wheel line is the reference one and it is generated as an ergodic stationary Gaussian random process based on a sum of harmonics :

$$r_L(x) = \sum_{k=1}^{N} \sqrt{2G_d(n_k)\Delta n} \cos{(2\pi n_k x + \theta_k)}, \tag{2}$$

in which N is the number of discrete spatial frequencies n_k in the range defined by the lower and the upper cut-off limits: $[n_1, n_N]$; Δn is the frequency resolution, in cycles/m; θ_k is a random phase angle uniformly distributed from 0 to 2π to generate a set of N_r independent profiles; $G_d(n)$ is the target one-sided PSD of displacements.

The parallel profile at the windward wheel line of the vehicle, which is spaced a distance $2b$ from the left one (Figs. 1(a) and (b)) is defined from [17] as:

$$\begin{aligned} r_W(x, y) = \sum_{k=1}^{N} \Bigg\{ & \sqrt{2G_{d,x}(n_k, y)\Delta n} \cos{(2\pi n_k x + \theta_k)} \\ & + \sqrt{2\left[G_d(n_k) - G_{d,x}(n_k, y)\right]\Delta n} \cos{(2\pi n_k x + \phi_k)} \Bigg\}, \end{aligned} \tag{3}$$

where ϕ_k is a random phase angle uniformly distributed between 0 and 2π and $G_{d,x}(n_k, y)$ is the one-sided cross PSD function, which is defined by accepting that the statistical properties of the road irregularities are the same in any direction (isotropy and homogeneity hypotheses) [17]:

$$G_{d,x}(n,y) = \int_{-\infty}^{\infty} 2R\left(\sqrt{\delta^2 + y^2}\right) \exp^{-i2\pi n\delta} \, \mathrm{d}\delta \qquad (4)$$

in which $R(\cdot)$ is the autocorrelation function of the pavement irregularity surface. Eq. (4) is particularised at $y = 2b$ to obtain the road profile at the windward wheel line.

The cross-slope of the deck is not considered when generating the pavement roughness in this work but it can be included in Eqs. (2) and (3) by shifting one of the two profiles. The irregularity profiles at the two wheel lines are generated on the entire length of the deck and on the two approaching platforms. In the proposed W-VBI framework these profiles are concatenated at the expansion joints of the abutments (Fig. 1(a)), where possible construction misalignments can be introduced if necessary. After obtaining the complete pavement profiles they can be filtered to obtain $\bar{r}(x, y)$ by means of the 'disk model' illustrated in Fig. 1(a). This model considers that the vehicle wheels have a certain radius (R_W), as it will be explained in Section 5.3.

Stage 2: Dynamic time-history analysis

This stage involves the *processing* of the coupled W-VBI analysis using the previous information about the bridge, the traffic and the environment. The dynamic response of the deck and the vehicles crossing the bridge is coupled through the tyre-pavement contact forces, with the additional wind forces acting on the deck and on the vehicles as shown in Fig. 1(b). The contact points of the vehicles change in time and it induces a dynamic action on the bridge that is added to the wind excitation. Assuming no loss of contact of the wheels, the response of the bridge can be decomposed in several single DOF systems that represent the contribution of relevant vibration modes of the structure. The displacement vectors of the bridge ($\mathbf{q}_b$) and of the vehicles ($\mathbf{q}_v$) can be defined in the coupled system of dynamics using modal coordinates and their time-derivatives:

$$\begin{bmatrix} \mathbf{M}_b & \mathbf{0} \\ \mathbf{0} & \mathbf{M}_v \end{bmatrix} \begin{bmatrix} \ddot{\mathbf{q}}_b \\ \ddot{\mathbf{q}}_v \end{bmatrix} + \begin{bmatrix} \mathbf{C}_b + \mathbf{C}_b^v & \mathbf{C}_{v,b} \\ \mathbf{C}_{b,v} & \mathbf{C}_v \end{bmatrix} \begin{bmatrix} \dot{\mathbf{q}}_b \\ \dot{\mathbf{q}}_v \end{bmatrix} + $$
$$\begin{bmatrix} \mathbf{K}_b + \mathbf{K}_b^v & \mathbf{K}_{v,b} \\ \mathbf{K}_{b,v} & \mathbf{K}_v \end{bmatrix} \begin{bmatrix} \mathbf{q}_b \\ \mathbf{q}_v \end{bmatrix} = \begin{bmatrix} \mathbf{\Phi}^{\mathrm{T}}(\mathbf{f}_{b,r} + \mathbf{f}_{b,w}) \\ \mathbf{f}_{v,g} + \mathbf{f}_{v,r} + \mathbf{f}_{v,w} \end{bmatrix}, \quad (5)$$

where $\mathbf{M}_i$, $\mathbf{C}_i$ and $\mathbf{K}_i$ are the mass, damping and stiffness matrices for the bridge and the vehicles, with $i = b$ and $i = v$, respectively. These matrices are constant in the entire W-VBI analysis. However, the coupling damping and stiffness matrices ($\mathbf{C}_{v,b} = \mathbf{C}_{b,v}$ and $\mathbf{K}_{v,b} = \mathbf{K}_{b,v}$, respectively) between the bridge and the vehicles, and the contribution of the vehicles to the damping and to the stiffness matrices of the bridge ($\mathbf{C}_b^v$ and $\mathbf{K}_b^v$) are time-dependent because they change with the position of the vehicles on the deck. This work utilises the W-VBI matrices given in Han *et al.* [13] adapted to the convention of positive forces and displacements included in Fig. 1(b). The forcing vector due to the moving wheel-pavement contact includes the effect of the pavement irregularities in the vehicle $\mathbf{f}_{v,r}$ and its counterpart in the bridge $\mathbf{f}_{b,r}$. They are obtained at each time-step by imposing the displacement profiles of the road at the tyre-pavement contact points. $\mathbf{f}_{v,g}$ represents the gravity force on the vehicles and $\mathbf{f}_{v,w}$ the wind forces and moments acting on them. These are obtained, respectively, from a steady approach as:

$$f_{v,w}^i = \frac{1}{2}\rho V_r^2 C^i(\psi) A_v, \quad f_{v,w}^j = \frac{1}{2}\rho V_r^2 C^j(\psi) A_v h_v, \tag{6}$$

where ρ is the density of the air; A_v and h_v are the reference surface of the vehicle and the distance between its centroid and the centroid of the deck (see Fig. 1(b)), respectively. The static coefficients C^i are related to the drag, side and lift forces on the vehicles $f_{v,w}^i$ ($i = D, S, L$, respectively) and C^j refer to the yaw, pitch and roll moments $f_{v,w}^j$ ($j = Y, P, R$, respectively). These coefficients depend on the instantaneous angle of incidence of the wind on the vehicles (ψ) given in Eq. (8). The resultant wind velocity acting on the vehicle (V_r) is a function of the instantaneous along-flow and along-drive wind speeds (u and v in Eq. (1)), and also of the vehicle speed (V):

$$V_r(t) = \sqrt{u^2(t) + (v(t) + V)^2}, \tag{7}$$

$$\psi(t) = \arctan\left(\frac{u(t)}{v(t) + V}\right). \tag{8}$$

The wind force vector on the deck $\mathbf{f}_{b,w}$ is applied to a simplified 3 DOF model of the cross-sections along its length, as shown in Fig. 1(b). In this model $\mathbf{f}_{b,w} = [f_{b,w}^D, f_{b,w}^L, f_{b,w}^M]^{\mathrm{T}}$ represents a vector with the drag, lift and moment components of the wind forcing at each node of the deck, respectively, and $\mathbf{q}_b = [p, h, \alpha]^{\mathrm{T}}$ are the corresponding generalised displacements.

13

The deck wind forces are obtained as a linear superposition of the mean, buffeting and self-excited forces, that is, $\boldsymbol{f}_{b,w} = \boldsymbol{f}_{b,w-s} + \boldsymbol{f}_{b,w-b} + \boldsymbol{f}_{b,w-se}$ [18, 19]. The mean wind forces are given as follows:

$$f_{b,w-s}^D = \frac{1}{2}\rho U^2 B C_D, \quad f_{b,w-s}^L = -\frac{1}{2}\rho U^2 B C_L, \quad f_{b,w-s}^M = \frac{1}{2}\rho U^2 B^2 C_M, \quad (9)$$

where B is the width of the deck; $C_D = C_D(\alpha_s)$, $C_L = C_L(\alpha_s)$ and $C_M = C_M(\alpha_s)$ are the static coefficients of the deck at the incidence angle between the wind and its section in static equilibrium α_s. The buffeting forces are obtained with the linear quasi-steady (LQS) model in which the fluid memory is neglected, and with it the aerodynamic admittance. Although this would effectively increase the buffeting forces, it can be argued that for bluff sections (such as those in most bridge decks) the aerodynamic admittance can be ignored [20]. The LQS model yields the following:

$$f_{b,w-b}^D = \frac{1}{2}\rho U^2 B \left(2C_D \frac{u}{U} + (C_D' - C_L)\frac{w}{U} \right),$$

$$f_{b,w-b}^L = -\frac{1}{2}\rho U^2 B \left(2C_L \frac{u}{U} + (C_L' + C_D)\frac{w}{U} \right), \quad (10)$$

$$f_{b,w-b}^M = \frac{1}{2}\rho U^2 B^2 \left(2C_M \frac{u}{U} + C_M'\frac{w}{U} \right),$$

in which $C_D' = C_D'(\alpha_s)$, $C_L' = C_L'(\alpha_s)$ and $C_M' = C_M'(\alpha_s)$ are the angle-derivatives of the static wind coefficients at α_s. Finally, the self-excited forces are obtained with the linear unsteady (LU) model:

$$f_{b,w-se}^D = \frac{1}{2}\rho U^2 B \left(KP_1^* \frac{\dot{p}}{U} + KP_2^* \frac{B\dot{\alpha}}{U} + K^2 P_3^* \alpha + K^2 P_4^* \frac{p}{B} + KP_5^* \frac{\dot{h}}{U} + K^2 P_6^* \frac{h}{B} \right),$$

$$f_{b,w-se}^L = \frac{1}{2}\rho U^2 B \left(KH_1^* \frac{\dot{h}}{U} + KH_2^* \frac{B\dot{\alpha}}{U} + K^2 H_3^* \alpha + K^2 H_4^* \frac{h}{B} + KH_5^* \frac{\dot{p}}{U} + K^2 H_6^* \frac{p}{B} \right),$$

$$\qquad\qquad\qquad\qquad\qquad\qquad\qquad\qquad (11)$$

$$f_{b,w-se}^M = \frac{1}{2}\rho U^2 B^2 \left(KA_1^* \frac{\dot{h}}{U} + KA_2^* \frac{B\dot{\alpha}}{U} + K^2 A_3^* \alpha + K^2 A_4^* \frac{h}{B} + KA_5^* \frac{\dot{p}}{U} + K^2 A_6^* \frac{p}{B} \right),$$

where $P^* = P^*(K)$, $H^* = H^*(K)$ and $A^* = A^*(K)$ are the flutter derivatives, dependent on the reduced frequency $K = \omega B/U$, for ω being the circular frequency of the bridge motion. Since Eqs. (11) are mixed relations including time- and frequency-dependent terms, a rational approximation is required to obtain pure time-domain representations of the wind forces acting on the deck during the W-VBI analysis. In this study, the rational approximation using indicial functions is used. The relations for obtaining the indicial functions from the flutter derivatives can be found in [18, 21]. It should be mentioned that the LU model used in the calculation of the self-excited forces in the time-domain allows to consider the fluid memory [22, 23]. This means that the wind forces depend on the previous time-history response, rather than simply considering the instantaneous bridge displacement as it was done in [6]. The LU model has been widely used in bridge aerodynamics and it proved to be consistent with aeroelastic Computational Fluid Dynamic (CFD) analyses [24, 25].

The W-VBI analysis is repeated for each of the N_r records of wind time-histories and pavement profiles generated in *Stage 1*. A discussion about the number of records to be included in the analysis is presented in this work.

Stage 3: Accident and comfort assessment - performance ratios η

The final step of the W-VBI framework is shown in Fig. 1(c), which involves the *post-processing* of the time-history results obtained in *Stage 2*. The safety and the comfort analyses are based on the arithmetic mean and the standard deviation (σ) of performance ratios (η) that are obtained for each of the N_r analysis runs performed. The safety or the comfort criteria are met for a particular wind and pavement record if $0 \leq \eta < 1$.

The driving safety assessment is based on the study of the pavement-wheel contact forces obtained from Eq. (5) in each time-step of the W-VBI analysis: $\mathbf{f}_{v,r} = [F_{c,Y-j}(t), F_{c,Z-j}(t)]^{\mathrm{T}}$. In this vector, $F_{c,i-j}$ are the contact forces at the vehicle wheels, with $i = Y, Z$ denoting forces in the transverse and in the vertical directions, respectively, and j being the position of the wheel or the group of wheels. These contact forces depend on the wheel-bridge dynamics as well as on the direct wind applied to the vehicle. Two types of accidents are considered in this work: overturning and side-slipping. The overturning accident is usually assumed to occur if any of the vehicle wheels lost contact with the pavement (i.e. $F_{c,Z-j} = 0$, for any j). However, instantaneous drops in the pavement irregularities at a single wheel can potentially unload it without implying a real overturn accident risk due to the stability provided

15

by the other wheels. For this reason the overturning accident in this work is based on the Load Transference Ratio (LTR) [6]:

$$\eta_{a,o} = \max_t \left[\left| \frac{F_{c,Z-L}(t) - F_{c,Z-W}(t)}{F_{c,Z-L}(t) + F_{c,Z-W}(t)} \right| \right], \tag{12}$$

in which $F_{c,Z-L}$ is the vertical force in all the leeward wheels ($F_{c,Z-L} = F_{c,Z-1} + F_{c,Z-3}$ in the 4-wheeled vehicle shown in Fig. 1(b)) and $F_{c,Z-W}$ is the vertical force in all the windward wheels ($F_{c,Z-W} = F_{c,Z-2} + F_{c,Z-4}$), respectively. If $\eta_{a,o} = 1$ all the lateral wind load is transferred to the leeward wheels and the vehicle is on the verge of an overturning accident.

Side-slip accidents occur if the lateral wheel forces exceed the frictional resistance of the tyre-pavement contact: $\mu_c F_{c,Z}$, where μ_c is the contact adherence. Establishing the risk of side-slip at each wheel separately is deemed too conservative because when the wheel with the smallest vertical force of an axle slips (usually the windward wheel) the total lateral force corresponding to that axle is resisted by friction in the opposite wheel (usually the leeward wheel of the axle). In order to account for this effect, in this work the risk of side-slip is defined as:

$$\eta_{a,s} = \max_t \left[\left| \frac{F_{c,Y-W}(t) + F_{c,Y-L}(t) - \mu_c F_{c,Z-W}(t)}{\mu_c F_{c,Z-L}(t)} \right| \right], \tag{13}$$

where $F_{c,Y-W}$ and $F_{c,Y-L}$ are the sum of the lateral forces at all the windward and the leeward wheels, respectively. The global accident risk is defined as the maximum between the overturning and the side-slip accident ratios: $\eta_{a,G} = \max(\eta_{a,o}, \eta_{a,s})$. Additionally, yaw-type vehicle accidents can be included in this framework, however, these are ignored here because their accurate assessment requires to include the driver's steering response to the lateral wind loads [3], which is out of the scope of this study.

The assessment of the bridge users' comfort is based on the recorded accelerations: $a_{i,j}(t)$, where i indicates the position where the acceleration is obtained ($i = v, b$ for the vehicle and the bridge deck, respectively) and $j = Y, Z$ represents the along-wind (transverse) and the vertical directions, respectively. Previous studies observed the importance of considering the frequency content of the acceleration in the assessment of the users' comfort, and not only its peak values [6, 8, 9]. In this work, the approach presented by Xu and Guo [4] to evaluate the comfort of the drivers is extended to consider also the pedestrians in the entire length of the sidewalks. The frequency

content of the acceleration time-history $a_{i,j}(t)$, in any direction and point of the deck and the vehicles, is obtained from the Root Mean Square (RMS) acceleration at different one-third octave bands as:

$$a_{\text{RMS}-i,j}(f_c) = \sqrt{\int_{f_l}^{f_u} S_{a_{i,j}a_{i,j}} \mathrm{d}f},$$ (14)

in which $S_{a_{i,j}a_{i,j}}$ is the PSD of the acceleration signal $a_{i,j}(t)$; f_l and f_u are the lower and the upper frequencies of each octave band, respectively. These can be expressed in terms of the corresponding central frequency (f_c) as: $f_l = 2^{-1/6}f_c$ and $f_u = 2^{1/6}f_c$.

According to the Irwin's comfort criterion [26], the vibrations perceived by the pedestrians on the deck are assessed from the RMS acceleration at different central frequencies f_c, which are compared with the corresponding admissible limits for those frequencies. The following ratio is introduced in this work to evaluate the risk of pedestrians' discomfort on the bridge:

$$\eta_{c,b-j} = \max_{f_c} \left[\frac{a_{\text{RMS}-b,j}(f_c)}{a_{\text{adm}-b,j}(f_c)} \right],$$ (15)

where $a_{\text{adm}-b,j}(f_c)$ is the admissible acceleration in frequent or in storm conditions; $j = Y, Z$ refers to the discomfort under lateral (along-wind) and vertical vibrations, respectively. The parameter $\eta_{c,b-j}$ is evaluated in the entire surface of the deck to account for the different positions in which the pedestrians may be located.

The evaluation of the vehicle vibration in the direction j is based on the frequency-weighted acceleration proposed by ISO 2631 [27]:

$$a_{w-v,j} = \sqrt{\sum_{k} (w_k a_{\text{RMS}-v,j}(f_k))^2},$$ (16)

where $a_{\text{RMS}-v,j}(f_k)$ and w_k are, respectively, the acceleration at the driver's seat (Point A' in Fig. 1(b)) and the weighting factor for the k-*th* octave band given in [27]. The combination of the vibration in the vertical and in the lateral directions follows the SRSS rule:

$$a_{w,v} = \sqrt{a_{w-v,Z}^2 + a_{w-v,Y}^2},$$ (17)

which is compared to the admissible vibration limit $a_{\text{adm}-v}$ established in [27] to obtain the risk of vehicle users' discomfort:

17
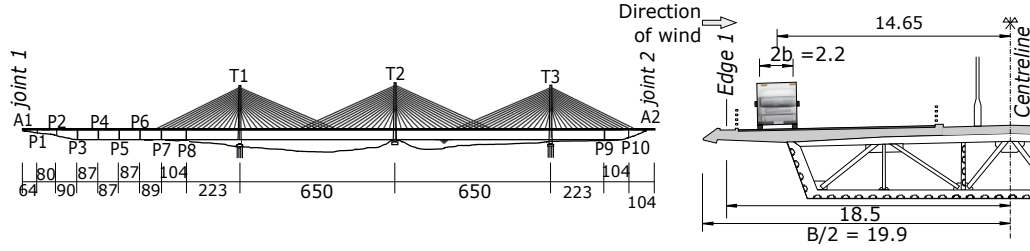
Figure 2: Elevation and deck cross-section of the Queensferry Bridge without wind barriers. Units in meters.

$$\eta_{c,v} = \frac{a_{w-v}}{a_{\mathrm{adm}-v}}. \tag{18}$$

3. Case study: the Queensferry Bridge

The proposed W-VBI analysis framework is applied to the study of the driving safety and the users' comfort in the Queensferry Bridge in Scotland. The structure is a continuous cable-stayed bridge with two main spans of 650 m each supported by a central plane of cables, as it is illustrated in Fig. 2. The 4.9-m deep cross-section of the cable-stayed deck is a metallic box closed by a 39.8-m wide concrete slab that holds 6 road lanes. The piers and the towers restrain the transverse and the torsional movements of the deck, but the vertical one is not constrained at the side towers (T1 and T3 in Fig. 2). The deck is fully fixed to the central tower (T2). This bridge was selected because its long deck (2643 m) facilitates the study of the dynamic interactions between the vehicles, the bridge and the wind. The aim is to obtain general conclusions on the W-VBI and not to assess the performance of any particular structure. For this reason the actual wind barriers in the Queensferry Bridge are ignored here in order to apply wind actions on the vehicles that would be representative of those in many other bridges without shielding.

The vibration properties of the bridge were extracted from a FE model developed in ABAQUS [28]. The deck and the towers were defined using a combination of beam elements and lumped masses rigidly connected to their centroids to represent the cable anchorages and other relevant dead loads. The typical length of the beam elements in the deck is approximately 10 m, which is adequate to capture its global response. The cables are modelled using single truss elements with reduced (Ernst) elasticity moduli to account

for cable-sag effects. The first vibration modes of the bridge are described in Table 1 and its fundamental mode shape is shown in Fig. 1(a). A preliminary study on the sensitivity of the W-VBI results to the number of vibration modes of the Queensferry Bridge showed that it is sufficient to include in the dynamic analysis (*Stage 2*) the first 82 modes that involve the movement of the deck (the local modes of the towers and the piers were removed from this selection). The frequency of the highest-order mode included in the analysis is 2.7 Hz. The structural damping ratio is constant and equal to $\xi = 0.5\%$ for all the modes, which is in agreement with EN 1991-2 [29] and with previous research works (e.g. [1, 3, 5]).

Table 1: First vibration modes in the Queensferry Bridge and in the vehicles. 'Wheel modes' refer to local vibration of the wheels.

	Mode	Description	Frequency [Hz]
Bridge	1	Vertical deck flexure	0.15
	2-4	Transverse tower flexure	0.15-0.17
	5	Transverse deck flexure	0.18
	7	Vertical deck flexure	0.25
	11	Torsion of the deck	0.40
Vehicle	1	Transverse movement	1.12
	2	Body heave	1.80
	3	Body roll	2.86
	4	Wheel and body pitch	3.29
	5-10	Wheel modes	3.64-5.45
	11	Body pitch	11.85
	12	Body roll	14.51

The traffic on the bridge consists of a convoy of 9 vehicles spaced at 70-m intervals. The total length of the convoy (650 m) is selected to load the complete length of the main spans at certain time instances of the analysis. The vehicles are centered on the closest lane to the upwind parapet of the deck (see Fig. 2) to maximise its torsional response. The vehicles considered are 8-m long rigid trucks with a total mass of 7500 kg. These vehicles combine large wind-exposed areas and driving velocities, which is critical for the safety and the comfort studies conducted. Each vehicle is represented in the W-VBI analysis by means of the 12 DOF model that is shown in Fig. 1(b). The aerodynamic coefficients of the vehicles are taken from [2]. Their mechanical properties are also taken from that work and they are included in Appendix A

for completeness (see Table 2). The reference area of the vehicles is $A_v = 10.5$ m^2 and their vibration modes are described in Table 1.

The wind velocity field is generated at each node of the FE model of the deck. In addition, the wind is generated at discrete points of two 340-m long approaching platforms in order to achieve a steady response in the vehicles before they access the deck and after they leave it. The wind on the vehicles is obtained at each instant by linear interpolation of the wind speeds at the adjacent nodes of the deck and the platforms. Without loss of generality, the wind simulation is based on integral turbulence lengths of 108, 54 and 30 m, and turbulence intensities (I_n) of 11%, 8% and 6% in the u_t, v_t and w_t components, respectively. The wind is generated using the von Karman's PSD and the coherence function included in Eq. (25) of the work of Solari and Piccardo [30]. The total duration of the simulated wind velocity records is 600 s, with a constant time-step of 0.01 s. The density of the air is $\rho = 1.25$ kg/m^3.

The static wind coefficients of the deck, as well as its H_l^* and A_l^* flutter derivatives (with $l = 1, 2, 3, 4$) were obtained using the verified CFD software VXflow [31, 32], based on the vortex particle method. The deck section was modelled in 2D with parapets but without vehicles and without wind barriers as it was already mentioned. Fig. 3(a) presents the static wind coefficients. A change of the moment derivative was observed between $\alpha_s = 2°$ and $4°$, which indicates aerodynamic stall. For this reason, the static wind coefficients were linearised in the $\pm 2°$ range of α_s. Fig. 3(b) shows the flutter derivatives corresponding to the torsional rotation of the deck and it includes their rational approximation. The remaining flutter derivatives were obtained from their quasi-steady counterparts.

The pavement irregularities were generated from the one-sided displacement PSD given by ISO 8608 [10]:

$$G_d(n) = G_d(n_0) \left(\frac{n}{n_0} \right)^{-2} \tag{19}$$

$n_0 = 0.1$ cycles/m being the discontinuity frequency. The value of the displacement PSD at n_0 defines the quality of the road; the following average values of $G_d(n_0)$ (in m^3/cycle) were employed in this work: $G_d(n_0) = 16 \times 10^{-6}$ for road type A (of very good quality) and $G_d(n_0) = 64 \times 10^{-6}$ for road type B (good quality). The road surface is generated with spatial frequencies between the cut-off limits $n_1 = 0.01$ and $n_N = 30$ cycles/m, with $\Delta n = 0.01$
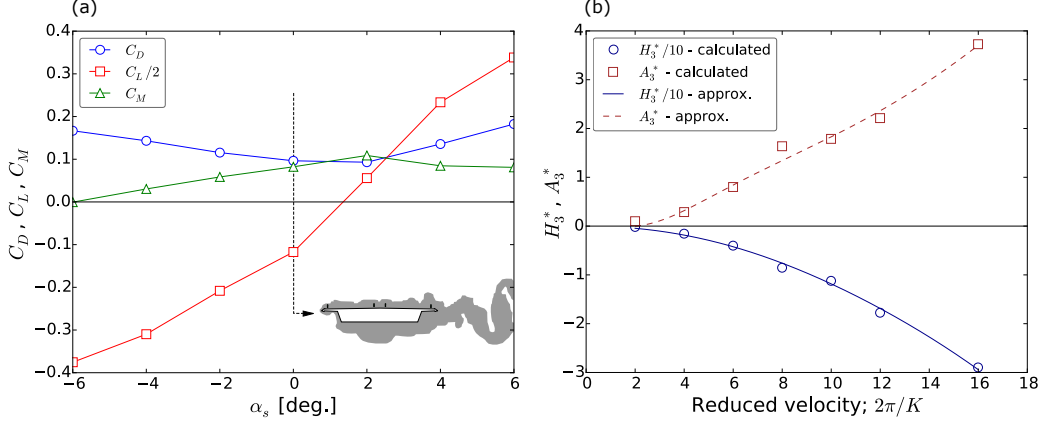
20

Figure 3: (a) Static wind coefficients of the deck and a time-frame of the CFD analysis for $\alpha_s = 0°$. (b) Flutter derivatives due to the torsional rotation of the deck, where the lines denote their rational approximation using indicial functions.

cycles/m. The spacing between consecutive points in the profiles is $\Delta r = 1$ cm, which provides enough accuracy in the frequency range below $n = 10$ cycles/m and it ensures at least three points of the pavement profile in each cycle of the upper cut-off frequency $n_N = 30$ cycles/m. The irregularity profiles are generated in the entire length of the deck and the two approaching platforms. The joints of the deck at the two abutments represented in Fig. 2 (A1 and A2) are defined as 1.92-m long perfectly flat segments in the pavement profiles. Fig. 4 shows one of these irregularity records applied at the leeward and at the windward wheel lines, as well as its detail at one of the bridge joints. This figure also compares the original profiles obtained with Eqs. (2) and (3) before and after applying the filter introduced by the tyre dimensions. The latter will be considered only in Section 5.3.

The system of dynamics in modal coordinates is solved by means of the Newmark-beta algorithm. In the post-processing of the results (Stage 3), the coefficient of lateral friction in the tyre-pavement contact is taken as $\mu_c = 0.9$ to represent good adherence with dry pavement conditions. The admissible limit of the vibration in the vehicle is $a_{\mathrm{adm,v}} = 1.2$ m/s^2, which corresponds to the geometric average of thresholds defining the uncomfortable vibration according to ISO 2631 [27].
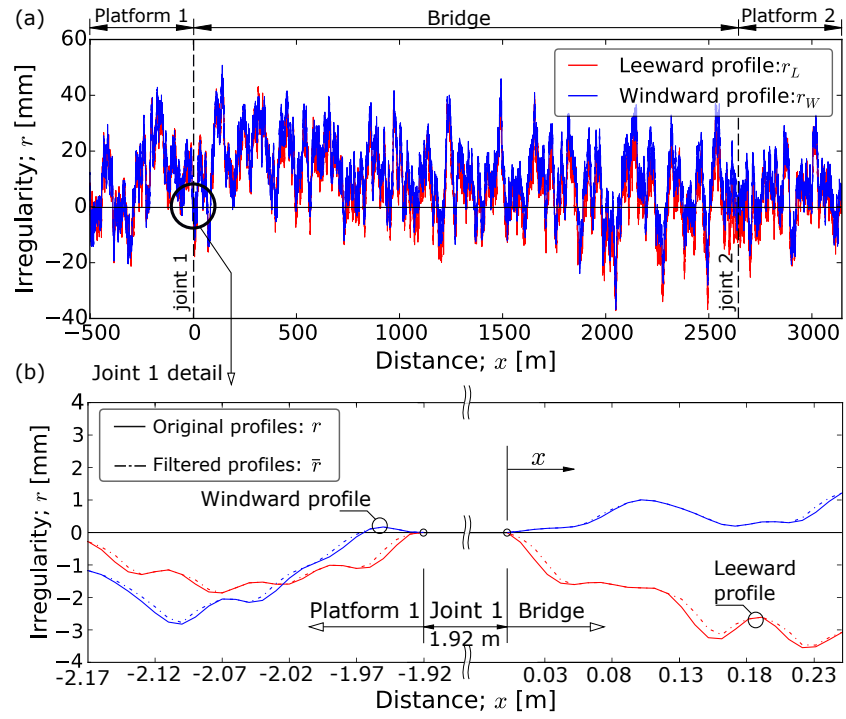
21

Figure 4: road type B irregularity profile record #1: (a) entire length of the deck and the platforms, (b) detail at the entrance of the bridge (joint 1).
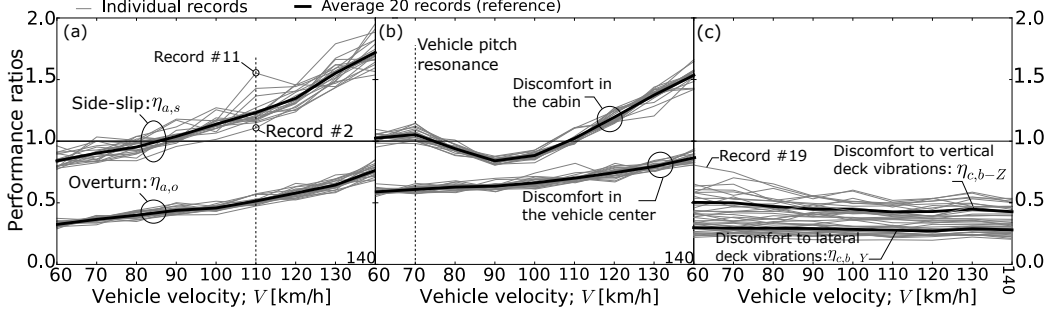
22

Figure 5: Peak performance risk ratios for all the vehicle velocities in a set of 20 wind and pavement records: (a) vehicle accident risks, (b) vehicle users' discomfort risk, (c) pedestrians' discomfort risk (storm conditions). Wind speed $U = 20$ m/s; road type A.

4. Effect of the record-to-record variability and the driving speed

Fig. 5 presents the peak driving and discomfort ratios obtained in any of the vehicles and the peak discomfort risk at any point of the deck for the complete range of driving velocities considered: $V = 60 - 140$ km/h, each 10 km/h. The thin lines in this figure correspond to the results obtained for 20 different pavement irregularity records and wind speed time-histories. These have a PSD of displacements $G_d(n_0)$ corresponding to road type A and a mean wind speed of $U = 20$ m/s, respectively, and their frequency contents also match the same target spectra. The only difference between these records is their randomness in the time and in the space domains. However, this introduces a significant variability in the vehicle and in the bridge responses as shown in Fig. 5. It is clear that considering the W-VBI results obtained from one single wind/pavement record may lead to results that are significantly different from other records or from the average of several analyses.

4.1. Statistical analysis

Fig. 5 shows the average from 20 records as a reference value, but it is interesting to study the degree of confidence associated with the average result in terms of the number of records included in its calculation (N_r). Because the probability distribution of the performance ratios is unknown, bootstrapping techniques [33] were used in this study. To this end, a total of 100 pavement and wind records were generated considering the road type A and $U = 20$ m/s, respectively. The performance ratios obtained

from the W-VBI analysis of each record were included in the sample vector $\boldsymbol{\eta} = [\eta_1, \eta_2, \cdots, \eta_{100}]$. A total of N_r results were randomly selected with replacement from $\boldsymbol{\eta}$ to obtain a bootstrap sample $\boldsymbol{\eta}^* = [\eta_1^*, \eta_2^*, \cdots, \eta_{N_r}^*]$, with $N_r \leq 100$. Each observed performance ratio in $\boldsymbol{\eta}$ has the same probability of being selected for $\boldsymbol{\eta}^*$ (in this case 1/100). The process was repeated 1000 times to obtain relatively smooth and stable confidence intervals [33]. The mean value of the performance ratios in the B_r-bootstrap sample $\boldsymbol{\eta}^*$ (with $B_r = 1, \cdots, 1000$) was computed for each size of the sample $N_r = 1, \cdots, 100$. This mean is referred to as the B_r-bootstrap replication and its 1000 random values for different N_r are included in Fig. 6. This figure illustrates that the bootstrap replications tend to oscillate around the mean value of the original 100-record sample $\boldsymbol{\eta}$, referred to as $\bar{\eta}^V$ in Fig. 6 (with $V = 60, 100, 140$ km/h). However, there is a significant variability of η for small N_r, particularly in terms of the discomfort in the deck.

Fig. 7(a) shows the variability of the mean of the global accident ratio obtained from 1000 bootstrap samples of increasing size N_r, with $V = 100$ km/h. The solid line represents the mean $(\bar{\eta}^*)$ of all the 1000 random bootstrap replications of $\bar{\eta}^{V=100}$, for each N_r. The dashed lines are the 2.5$^{\text{th}}$ and the 97.5$^{\text{th}}$-percentiles of the bootstrap distribution: $\bar{\eta}^{*(2.5\%)}$ and $\bar{\eta}^{*(97.5\%)}$, respectively. The range between these lower and upper bound limits represents the 95%-confidence interval of the mean value of the performance ratio: $W_{95} = \bar{\eta}^{*(97.5\%)} - \bar{\eta}^{*(2.5\%)}$. The value of $\bar{\eta}^*$ is almost independent of N_r, for all the driving speeds and performance ratios considered. However, the width of the confidence intervals decreases significantly by increasing N_r, particularly from 1 to 20 records. Considering a single record there is a 95%-confidence that the global accident ratio will be between 1.01 and 1.31 (i.e. $W_{95} = 0.3$) for the case examined in this figure, but considering the average of 20 records 95% of the cases the result will be between 1.11 and 1.17 (i.e. $W_{95} = 0.06$). Fig. 7(a) also shows the histograms of the probability density distribution for the bootstrap replications with different N_r. Considering small samples ($N_r = 1$ in the limit) leads to a very non-normal distribution, and it has been observed that for this and for other performance ratios the mean value $\bar{\eta}^*$ is closer to the 2.5$^{\text{th}}$-percentile than to the 97.5$^{\text{th}}$-percentile. This supports the use of bootstraping techniques to obtain W_{95} instead of standard normal distribution tables. In agreement with the central limit theorem, as N_r increases the histogram becomes closer to a normal probability distribution.

The width of the 95%-confidence interval is normalised in order to facilitate the comparison between different performance ratios and driving speeds:
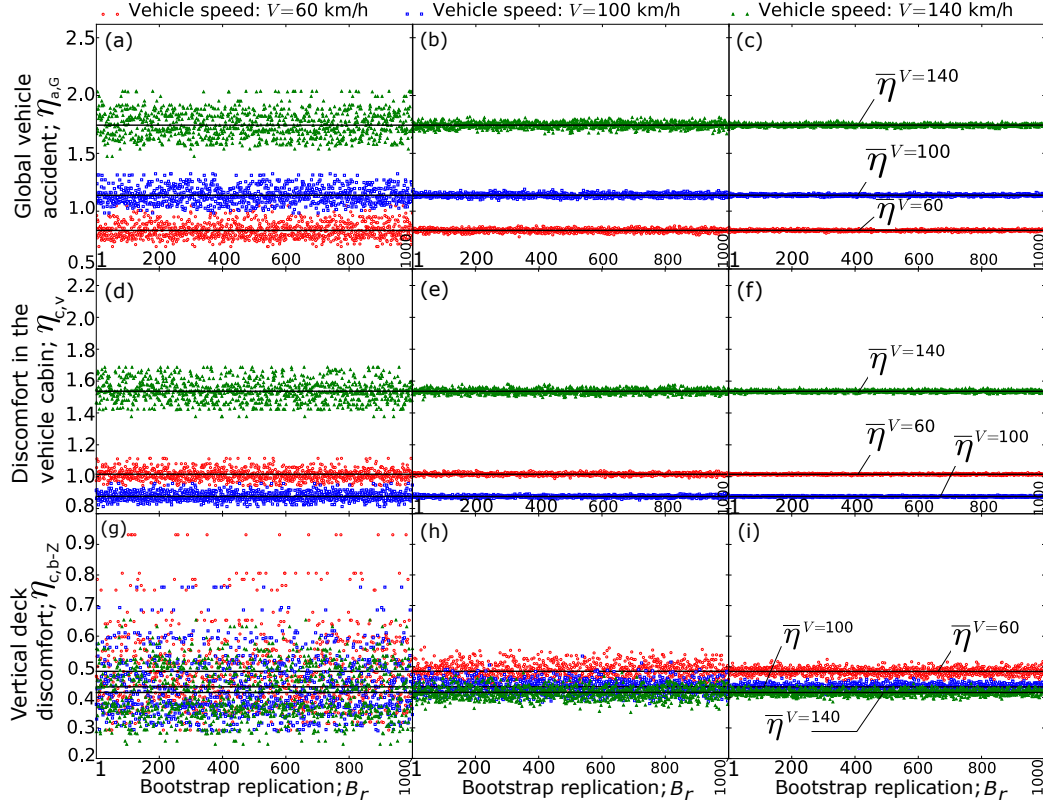
24

Figure 6: Random realisations of the peak performance risk ratios in bootstrap samples of different size (i.e. with different number of records N_r included): (a,b,c) global vehicle accident risk with (a) $N_r = 1$, (b) $N_r = 20$, (c) $N_r = 100$; (d,e,f) vehicle users' discomfort risk with (d) $N_r = 1$, (e) $N_r = 20$, (f) $N_r = 100$; (g,h,i) vertical pedestrians' discomfort risk (storm conditions) with (g) $N_r = 1$, (h) $N_r = 20$, (i) $N_r = 100$. Wind speed $U = 20$ m/s; road type A.
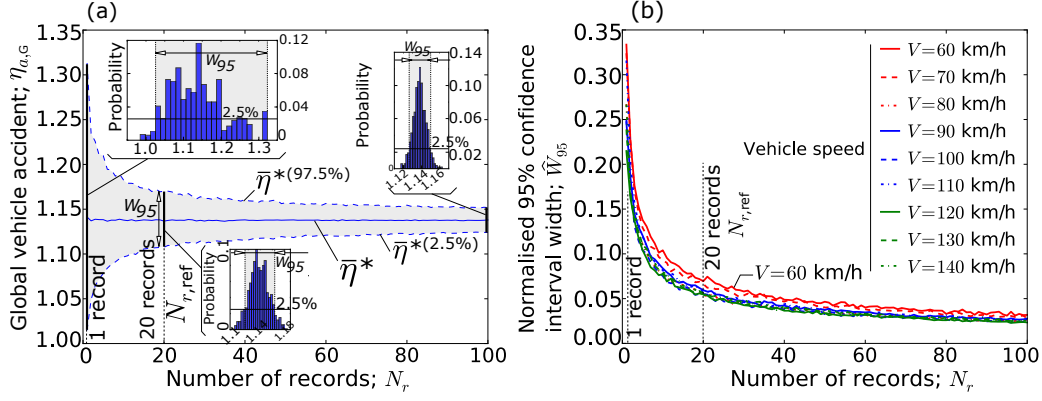
Figure 7: Confidence in the peak global vehicle accident risk with different sample sizes: (a) mean value of $\eta_{a,G}$ with $V = 100$ km/h and 95%-confidence intervals, (b) normalised 95%-confidence interval width. Wind speed $U = 20$ m/s; road type A.

$$\hat{W}_{95} = \frac{W_{95}}{\bar{\eta}^*} = \frac{\bar{\eta}^{*(97.5\%)} - \bar{\eta}^{*(2.5\%)}}{\bar{\eta}^*} \qquad (20)$$

The values of $\hat{W}_{95}$ for the global accident ratio are included in Fig. 7(b). Although the driving speed affects the variability in the vehicle safety assessment, in all the cases the reduction of the confidence interval with increments of N_r seems to be logarithmic. This is confirmed in Fig. 8, where the plots of the maximum $\hat{W}_{95}$ for any value of V considering increasing N_r appear as nearly straight lines in logarithmic coordinates, regardless of the performance ratio considered. These results will be discussed in detail in the following sections.

4.2. Driving accident risk

Fig. 5(a) shows that the risk of vehicle overturn changes slightly from record to record, and this difference generally increases with the vehicle velocity. However, the record-to-record variability is much more pronounced in terms of the side-slip accident risk, which dominates the driving instability when the mean wind speed is 20 m/s in this study. The results indicate that considering a single record ($N_r = 1$) in the analysis, which is a common practice in W-VBI research works, can lead to a significant misinterpretation of the global accident ratio. In this particular case, the side-slip risk ratio for a driving speed of $V = 110$ km/h is $\eta_{a,s} = 1.6$ for record #11, which is 40%
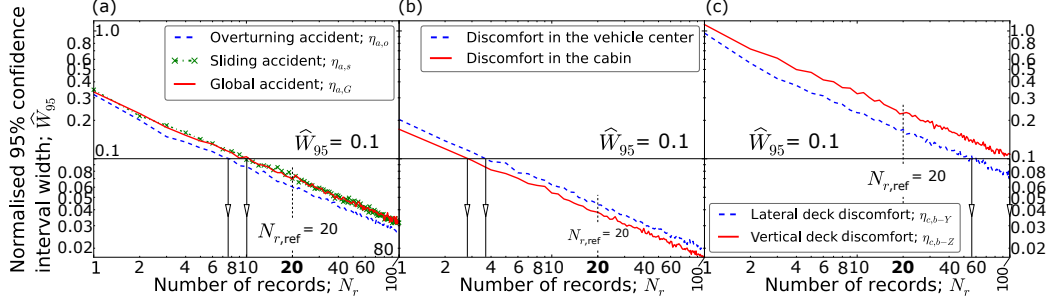
26

Figure 8: Normalised 95%-confidence interval width for the performance ratios related to the: (a) vehicle accident η_a, (b) vehicle users' discomfort $\eta_{c,v}$, (c) pedestrians' discomfort $\eta_{c,b}$. Wind speed $U = 20$ m/s; road type A.

higher than the one obtained in the same conditions with record #2. Considering the response of the vehicle at the lowest driving speed ($V = 60$), Fig. 6(a) shows that when the assessment is based on a single record ($N_r = 1$) the risk of vehicle accidents can be underestimated by 15% with respect to the average of the results from 100 records ($\bar{\eta}^{V=60}$), or it can be overestimated by up to 20% and eventually indicate the occurrence of an accident that $\bar{\eta}^{V=60}$ does not predict.

In order to explain this result, Fig. 9(a) presents the evolution of the accident risk ratios in time-domain for vehicle 9 (the last one in the convoy) and record #11. The figure highlights the interval of highest risk of vehicle accidents that is responsible for the peak observed in Fig. 5(a) for $V = 110$ km/h. The instants t_{A1}, t_{T1}, t_{T2}, t_{T3} and t_{A2} represent the moments in which the centroid of vehicle 9 passes the left abutment (A1), the three towers (T1, T2 and T3) and the right abutment (A2), respectively. The results indicate that the side-slip accident risk increases when the vehicle is on the bridge, which is attributed to the lateral oscillation of the deck. However, the vertical vibration of the deck does not increase significantly the risk of vehicle overturning. Fig. 9(b) zooms in the period of high accident risk. The different time instants t_O and t_S denote the moments in which the risk of vehicle overturning and side-slip present local maxima, respectively. The peaks corresponding to both types of accident risk alternate in time. It is noted that the consecutive peaks of the same type of driving instability are spaced at approximately 1-s intervals, i.e. 1-Hz frequency, which is close to the 1.12-Hz frequency of the first lateral vibration mode of the vehicle (see Table 1). This indicates that the accident risk is dominated by the transverse
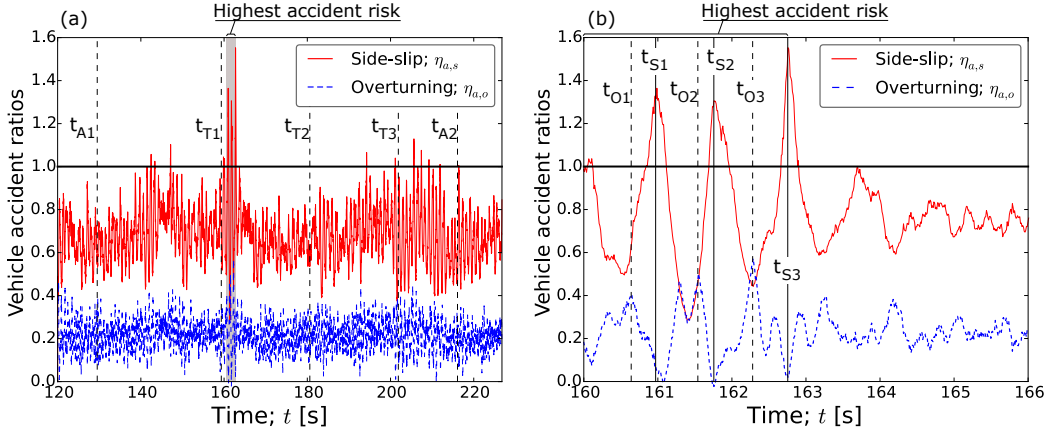
27

Figure 9: Overturning and side-slip accident ratios for the vehicle 9: (a) complete time-history obtained as the vehicle crosses the bridge, (b) detail of a time-interval in which the accident risk is high. Wind speed $U = 20$ m/s; vehicle speed $V = 110$ km/h; road type A; record #11.

motion of the vehicle excited by the lateral wind.

Fig. 10 compares the time-history of the wind side force on the vehicle 9 ($f_{v,w}^S$) with the pavement irregularities and with the reactions at the wheels of this vehicle at each instant of the analysis considering the record #11. Fig. 10(c) shows that the vertical wheel reactions are similar when the vehicle is off the bridge and when it is on it, which confirms that the influence of the vibration from the deck is less significant for the vehicle than the direct wind forces and the pavement irregularities applied to it. The comparison between Figs. 9(a) and 10(a) indicates that the intervals of large wind side forces on the vehicle due to wind gusts are connected with the intervals in which the side-slip risk is higher. However, the largest accident risk and the minimum vertical wheel reaction forces are obtained during a short interval of time in which the wind-induced force is relatively high but it is not the largest one observed during the whole journey of vehicle 9 (see Fig. 10(a)). The highest accident risk is obtained soon after the vehicle 9 passes the first tower (t_{T1}), however, this is not due to the sudden change in the aerodynamic forces when the vehicle crosses the wake of the tower because this is not modelled in the W-VBI analysis. The movement of the deck and the vibration that it induces in the vehicles are also reduced close to the towers. Consequently, the explanation for the increment in the accident risk close to t_{T1} must be in the wind and in the pavement records. Fig. 10(d) details the wind side force

28

on the vehicle during the interval in which the accident risk is larger. The wind gust that appears in record #11 at $t = 160.6$ s and at the position of the vehicle is responsible for the first peak in the overturning accident risk in this interval (t_{O1}). Fig. 10(f) shows that the increase of the side force on the vehicle unloads the windward wheels, especially the rear one (wheel 4), which increases the overturning risk expressed in Eq. (12). The side-slip risk at t_{S1} occurs when the vehicle passes completely the wind gust and the side force is reduced to a value that is close to the one induced by the mean wind speed (36.9 kN when $U = 20$ m/s and $V = 110$ km/h). At this particular instant the vehicle moves laterally in the opposite direction to the wind force and the windward wheels are loaded, which reduces the risk of overturning. However, the rear leeward wheel (wheel 3) is significantly unloaded due to the lateral oscillation of the vehicle, which combined with the side force exerted by the wind increases the side-slip risk given by Eq. (13) at t_{S1}.

Consequently, the lateral oscillation of the vehicle with 1.12-Hz frequency explains why the risk of side-slipping is maximum when the possibility of overturning is minimum (and vice-versa) in Fig. 9(b). That figure also shows that the third peak of the overturning ratio (at t_{O3}) and, especially, the side-slip ratio (t_{S3}) is the largest one in the whole journey. This is explained by two problematic effects that are combined in the wind/pavement record #11 with $V = 110$ km/h: (1) the peaks of the wind side force on the vehicle in the period of highest accident risk are spaced at approximately 1-s intervals, which combined with the lateral frequency of the vehicle starts building up a resonant effect that adds energy to the vehicle response until it reaches the maximum at the third peak (t_{O3} and t_{S3}); (2) when the third peak occurs the front wheels are passing depressions of the pavement surface (see Fig. 10(e)) that instantaneously unload the wheels and increase the accident risk, this is especially significant in the front windward wheel (wheel 2) at t_{O3}, as shown in Fig. 10(f).

The results demonstrate that certain driving speeds can position the vehicle at unfavourable locations of the deck in which the combined effect of the pavement irregularity and the wind gusts lead to situations of potential driving accidents. Fig. 5(a) shows that the wind and the pavement record #11 is unfavourable for a driving speed of 110 km/h, but for the same record the vehicle is more stable at higher driving speeds because it avoids unfavourable combinations of the wind and the pavement irregularities. Therefore, it is important to consider a sufficient number of records in order to obtain statistically meaningful results from the point of view of the vehicle stability
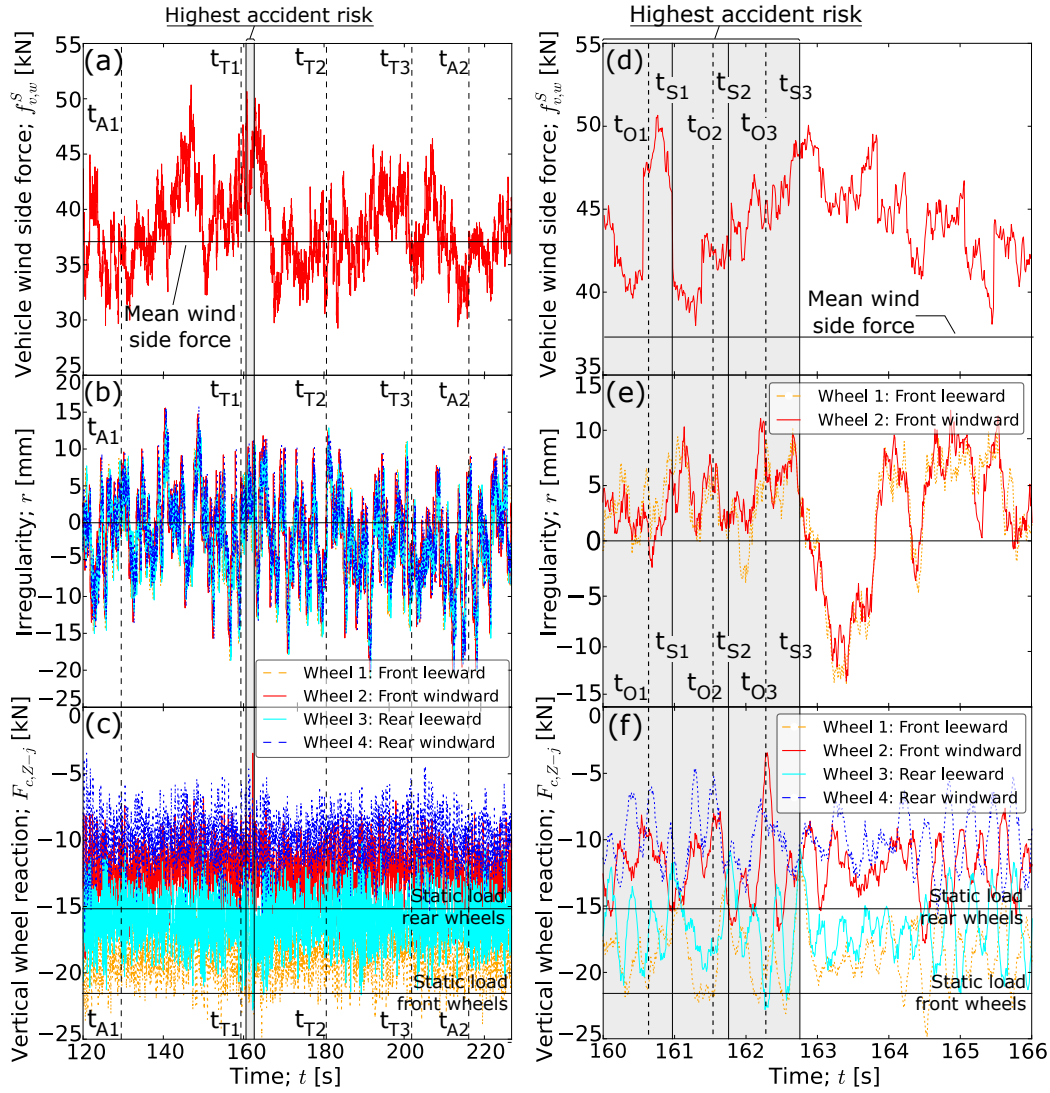
29

Figure 10: (a) wind side force acting on the vehicle, (b) pavement irregularity at the wheels, (c) vertical reaction forces at the wheels. Figs. (d) to (f) present at detail of Figs. (a) to (c) focusing on the time-interval in which the accident risk is the highest. Vehicle 9; wind speed $U = 20$ m/s; vehicle speed $V = 110$ km/h; road type A; record #11.

assessment.

It has been observed that any combination of 10 or more different records (i.e. $N_r \geq 10$) gives an average accident ratio that increases for any increment of the vehicle velocity, unlike the case with $N_r = 1$ as shown in Fig. 5(a). Comparing Figs. 6(a) to (c) it is clear that increasing N_r leads to results that are closer to the average of 100 records, although the variability of the results seems to be proportionally larger at low driving speeds. This is verified in Fig. 7(b), which shows that the normalised width of the confidence interval ($\hat{W}_{95}$) is reduced significantly by increasing N_r in small samples, but it changes at a slower rate for $V = 60$ and 70 km/h. This is attributed to the fact that the slower the driving speed the more likely is that the vehicle is affected by wind gusts when crossing the bridge. Considering $N_r > 20$ reduces marginally the variability of the mean response and this number of records will be adopted as the reference in the present work ($N_{r,\text{ref}} = 20$). However, it is interesting to compare the influence of N_r on $\hat{W}_{95}$ for different types of vehicle accident in Fig. 8(a). The dispersion of the overturning accident ratio is smaller than that for the sliding accident, which can be attributed to the contribution of the lateral movement of the studied bridge to the transverse wheel reactions. Establishing $\hat{W}_{95} = 0.1$ as a reasonable accuracy limit the number of records to be considered in the analysis of the driving safety should be at least 10. This result is affected by the pavement irregularities and it is valid for 'good quality roads'. In a perfectly flat road $\hat{W}_{95}$ can be reduced by approximately 25% when $U = 20$ m/s.

4.3. Vehicle users' discomfort risk

Fig. 5(b) compares the driving velocity with the discomfort risk for the users of the vehicles ($\eta_{c,v}$) at their centroids (point A in Fig. 1(b)) and at the drivers' seats (point A', spaced transversely a distance $b_d = 0.8$ m from the mid plane of the vehicle), for 20 different records. Like in the case of the vehicle accident risk, certain driving speeds and records amplify or reduce appreciably the vehicle vibration. However, the record-to-record variability in the driving comfort assessment is smaller than the one for the vehicle stability, which is also confirmed in the 1000 bootstrap replications presented in Fig. 6(d). The vehicle vibration obtained from just one record ($N_r = 1$) may be above or below the admissible limits depending on the randomness of the pavement and the wind histories, but the mean value of samples with larger N_r is much less sensitive to the record-to-record variability (Figs. 6(e) and (f)). This is visualised in Fig. 8(b), which shows that the mean vehicle

discomfort ratio obtained from 4 or more records has a relatively narrow 95%-confidence interval ($\hat{W}_{95} < 0.1$) at any location within the vehicle. The results indicated that V does not affect significantly the value of $\hat{W}_{95}$. It is also observed that the influence of the pavement irregularities on the record-to-record variability is small because the maximum error is similar with a perfectly smooth road or with the road type A.

It is interesting to note in Fig. 5(b) that the discomfort ratio at the vehicle's cabin is significantly larger than at its centroid, although the record-to-record variability is smaller. Indeed, the acceleration recorded at the cabin of the vehicle exceeds the admissible value for most of the driving velocities when the mean wind speed is 20 m/s. This is due to the vertical vibration introduced by the pitching motion of the vehicle, which is not present at the centroid of the truck but it affects significantly the vibration at the drivers' seat due to the relatively long distance between the cabin and the centroid of the vehicle ($L_c = 3$ m in Fig. 1(b)). This is especially significant when the driving speed is $V = 70$ km/h and it is not due to the wind action because it is observed with and without it.

To explore this effect further, Fig. 11 shows for one particular record the PSD of the vertical and the lateral accelerations in the driver's seat of the first vehicle crossing the bridge at 70 and 90 km/h (with road type A and $U = 20$ m/s). In both cases the lateral vibrations dominate the response in the low frequency range, below 1.5 Hz, with the clear contribution of the first vibration mode of the vehicle at 1.12 Hz, which corresponds to the lateral motion of the vehicle box. There is also a moderate contribution of the first body roll mode of the vehicle (2.86 Hz, mode 3) to the wind-induced lateral vibration. The vertical motion of the cabin is dominated by the vehicle vibration modes above 1.5 Hz, with two distinct peaks: the first one due to the body heave mode (1.8 Hz, mode 2) and the second one corresponding to the pitching motion of the wheel and the body masses in the vehicle model (3.29 Hz, mode 4). It is well known that the pavement irregularities applied at the vehicle wheels affect the contribution of the vertical modes of the vehicle to the vibration and the comfort assessment [9, 11]. The amplitude of such irregularities depends on the road quality but the frequency (f) with which they are applied at the vehicle wheels depends also on the driving speed (V) according to the expression: $f = nV$, where n refers to the spatial frequency of the road under consideration. When the vehicle circulates at 70 km/h the low-order pavement irregularity frequencies at the wheels are close to the first vehicle pitching frequency ($f = 3.29$ Hz) and amplify the PSD of
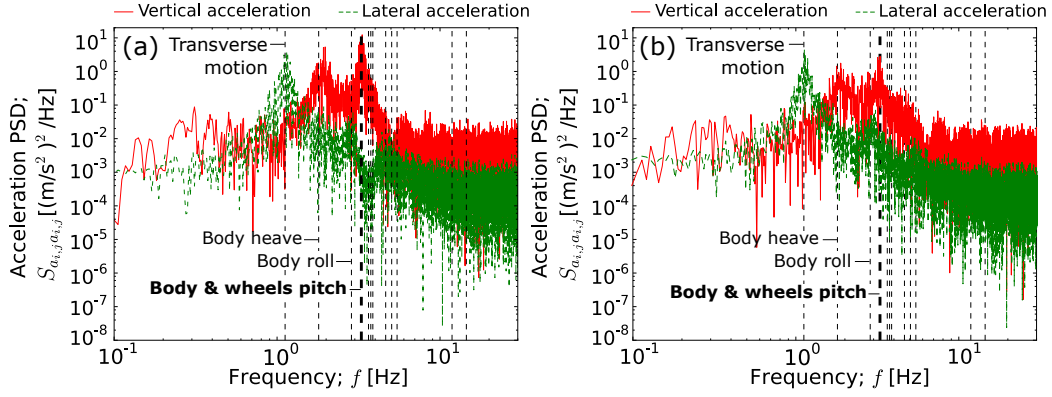
Figure 11: PSD of the acceleration at the drivers' sit when the vehicle crosses the bridge at: (a) $V = 70$ km/h, (b) $V = 90$ km/h. The vertical lines indicate the vibration frequencies of the vehicle (Table 1). Vehicle 1; wind speed $U = 20$ m/s; road type A; record #1.

the acceleration shown in Fig. 11(a) for this frequency. This is responsible for the discomfort at the vehicle cabin at 70-km/h driving speed. It is a pavement-induced resonant effect of the vehicle that is associated with a de-amplification of the wind-induced lateral motion of the cabin at the same frequency (3.29 Hz). However, if the vehicle crosses the bridge at a higher speed (e.g. 90 km/h) the spatial road irregularities are applied at the wheels with higher frequencies (f) that are not coupled with the pitching mode of the vehicle. This is the reason why the vertical acceleration PSD for $V = 90$ km/h in Fig. 11(b) shows a reduced contribution of the cabin pitch motion. It should be mentioned that the pitching resonance at low driving speeds does not have influence on the driving stability, as shown in Fig. 5(a), and it may not occur in other types of vehicles in which the distance from their centroid to the driver's seat is smaller (e.g. cars).

4.4. Pedestrians' discomfort risk

Fig. 5(c) presents the record-to-record variability in terms of the maximum discomfort ratio for pedestrians located at any point of the entire deck. The admissible values of the vibration are given by the Irwin's criterion for storm conditions, which is consistent with the high wind velocity that corresponds to the results in Fig. 5: $U = 20$ m/s. In this case all the records result in admissible vibrations in the deck ($\eta_{c,b} < 1$), both in the vertical and (especially) in the lateral directions. However, the dispersion of the results for different records is large, particularly for the vertical vibration of

33

the deck at low driving speeds. Fig. 6(g) clearly shows the large influence of the wind/pavement randomness on the risk of pedestrians' discomfort, with deviations of up to 90% with respect to $\bar{\eta}^V$. Comparing this with the results in Fig. 6(h) it can be seen that the mean values of 20-record samples reduce significantly the problem. However, even considering $N_r = 100$, with the significant computational cost that it represents, leads to some variability in the mean response (Fig. 6(i)), which is also illustrated in Fig. 8(c). Increasing N_r reduces $\hat{W}_{95}$ for the pedestrians' discomfort at a slower rate than in the case of the vehicle response ratios. As a result, a large number of records is required to obtain a relatively narrow confidence interval for the mean acceleration of the deck, particularly in the vertical direction which requires $N_r \geq 100$ to obtain $\hat{W}_{95} \leq 0.1$ with a road type A and regardless of V (smaller $\hat{W}_{95}$ is obtained without pavement imperfections).

However, the goal of this study is not to evaluate the SLS of vibrations in a particular bridge. The results obtained with the mean of 20 records allow to obtain information about the role of the pavement and the wind on the pedestrians' comfort levels. Fig. 5(c) shows that the 20-record average of the pedestrians' discomfort ratio to the lateral deck vibrations is almost insensitive to the driving speed of the vehicles. This is because the lateral vibration of the deck is mainly induced by the side wind force and not by the traffic actions. The risk of discomfort to vertical accelerations in the deck is slightly influenced by the velocity of the vehicles due to the traffic-induced vibration. This is clear in the response of the deck for particular records, such as record #19, in which the discomfort ratio is significantly large when $V = 60$ km/h and it is reduced to values that are closer to the 20-record average for larger driving speeds.

In order to explain this result, Fig. 12(a) presents the peak vertical discomfort ratio along the entire length of the deck for the pavement and the wind record #19. The results distinguish between the centreline of the deck and the position where the lateral sidewalks are located according to Fig. 2: Edge 1 with 18.5-m eccentricity, and Edge 2 in the opposite (symmetric) side. The vertical vibration and the discomfort risk increase between the piers and the towers that support the deck. In the left region of the deck before the cable-system, between the left abutment (A1) and the pier P7, the vertical acceleration at the girder centreline is almost the same as that at the Edges 1 and 2 because of its moderate torsional response. However, the torsional flexibility increases in the cable-stayed region of the bridge (P7-P10), where the vertical vibration and the discomfort at the edges are significantly larger

than at the center of the deck. This may be favoured by the central cable-plane system of the Queensferry Bridge. The piers and the towers restrain the torsional movement of the deck in the studied structure and at these locations the discomfort ratio is the same across the girder, however, the side towers (T1 and T3) allow the vertical movement of the deck. This type of distribution of the vibration along the deck is also observed for other records and vehicle velocities. Nevertheless, according to Fig. 12(a) what makes the maximum discomfort of the deck significantly larger for record #19 and $V = 60$ km/h is the vertical vibration at the edges of the deck in the first cable-stayed span, between the piers P7 and P8.

This effect is due to the amplification of the torsional response of the deck. Fig. 12(b) shows the RMS vertical acceleration at the midpoint between piers P7 and P8, where the vibration is maximised for record #19 and $V = 60$ km/h. The RMS acceleration is obtained in a wide range of one-third octave bands using Eq. (14) and it is compared with Irwin's comfort limits for frequent and storm conditions. It is observed that the vertical RMS acceleration in the center of the deck is dominated by frequencies between 1 and 2 Hz in which the human sensitivity to vibrations is maximum. However, at the center of the girder the pedestrians would not feel discomfort, even if crossing the bridge with a 20-m/s mean crosswind could be considered as a 'frequent' situation. The vibration changes at the edges of the deck, where the sidewalks are normally located. At these points the vertical acceleration exceeds the admissible limit for frequent vibrations because of the contribution of a 2.2-Hz frequency vibration mode of the bridge involving a coupled torsion/transverse-flexural mode of the side spans of the deck. This mode is also shown in Fig. 12(b).

It should be noted that in this work the study of the pedestrians' comfort is based only on the bridge vibrations, and the influence of the direct wind on the pedestrians is ignored. However, the importance of Fig. 12 is not in the magnitude of the pedestrians' discomfort (which is largely subjective) but rather in the observation that points of the bridge different from midspan may be critical. Therefore, the full length of the deck needs to be included in the assessment of the pedestrians' comfort, and not simply one point as it was done in previous W-VBI works [6]. It has been also observed that the pavement irregularities do not play a significant role in the vibration of the deck in this bridge.
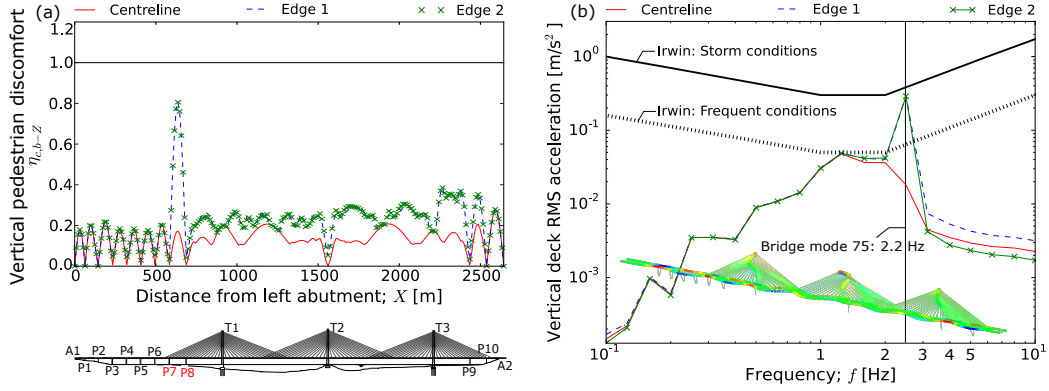
Figure 12: (a) Peak pedestrians' vertical discomfort ratio ($\eta_{c,b-Z}$) along the deck, (b) frequency content of the vertical acceleration at the midpoint of the deck between piers P7 and P8. $V = 60$ km/h; $U = 20$ m/s; road type A; record #19.

5. Effect of the tyre-pavement characteristics

This section explores the effect of the pavement characteristics and the tyre dimensions on the W-VBI response. From the previous discussion the results are based on the 20-record arithmetic mean ($N_r = N_{r,\text{ref}} = 20$). In the following figures the mean response ($\bar{\eta}$) is represented with lines or with markers, and the dispersion with coloured bands that have a total width of two standard deviations (2σ). Fig. 7(a) indicated that the 20-record mean is almost centered in the probability distribution, for this reason the 2σ-band is presented as centered in $\bar{\eta}$.

5.1. Road pavement quality

The influence of the pavement quality is studied for different vehicle and wind speed levels in the form of Critical Wind Curves (CWC). These plot for each mean wind velocity (U) the critical driving speed (V_C) beyond which accidents or discomfort occur (i.e. $\eta = 1$). For any value of U, the vehicle speed (V) was increased from 60 to 140 km/h, in 10-km/h increments, and V_C was obtained by linear interpolation between the largest value of V for which $\eta < 1$ and the lowest with $\eta > 1$. If the lowest driving speed ($V = 60$ km/h) gives $\eta > 1$ the value of V_C is set as 0 km/h on the safe side. On the other hand, V_C is considered as non-existing when the maximum vehicle velocity ($V = 140$ km/h) yields $\eta < 1$. In the case in which two different vehicle velocities satisfy that $\eta = 1$ (e.g. Fig. 5(b)) the lowest value is selected.

Fig. 13 presents the CWC for different road qualities. The pedestrian discomfort is not considered here because it is not affected by the driving speed. Fig. 13(a) shows that the global vehicle accident risk ($\eta_{a,G}$) is strongly increased as the pavement quality is deteriorated. This affects both the overturning and the side-slip accidents, and it is due to the reduction of the wheel reaction forces at certain instants of the vehicle's journey by increasing the pavement irregularity amplitudes. For example, considering a mean wind speed of 20 m/s the average value of V_C is 91 km/h in the ideal case in which the road is perfectly flat, but this velocity is reduced in road types A and B by 8.3% ($V_C = 84$ km/h) and by 117% ($V_C = 42$ km/h) with respect to the flat pavement, respectively. In addition, vehicle accidents with resonable driving speeds are only observed in the road with the lowest quality (road type B) when U is between 10 and 15 m/s. This range of wind speeds is relatively low and it should be noted that the quality of road type B is categorised by ISO 8608 [10] as 'good'. On the other hand, reducing the driving speed always improves the vehicle stability, especially under high winds. It is observed that this is mainly because of the reduction of the relative speed V_r in Eq. (7), which decreases quadratically the side force and moments on the vehicle given in Eq. (6). However, accidents are always observed when the mean wind speed is $U = 25$ m/s, regardless of the vehicle speed (with $V \geq 60$ km/h) and of the road quality.

The influence of the pavement quality on the comfort of the vehicle users is presented in Figs. 13(b) and (c). These two plots show the combinations of wind and driving speeds for which the ride is considered as comfortable or uncomfortable ($\eta_{c,v}$) by a person located at the centroid or at the cabin (driver's seat) of the vehicle, respectively. It is observed that at the cabin it is much easier to feel discomfort due to the influence of the pitching motion, but in both cases the risk is significantly higher the worse the road quality and the larger the driving and the wind speeds are. At the centroid of the vehicle (Fig. 13(b)), only the largest wind speed ($U = 25$ m/s) can make the ride uncomfortable with a perfect road if the driving speed is above $V_C = 115$ km/h, but in road types A and B this value is reduced by 8.5% ($V_C = 106$ km/h) and by 219% ($V_C = 36$ km/h) with respect to the flat pavement, respectively. The influence of the road irregularities on the comfort is even more critical at the driver's seat due to the pitching motion induced by the pavement (see Fig. 13(c)). In the absence of pavement irregularities (perfect road) only the highest wind speed would result in significant discomfort at the driver's seat ($V_C = 70$ km/h), but on a road of 'very good' quality
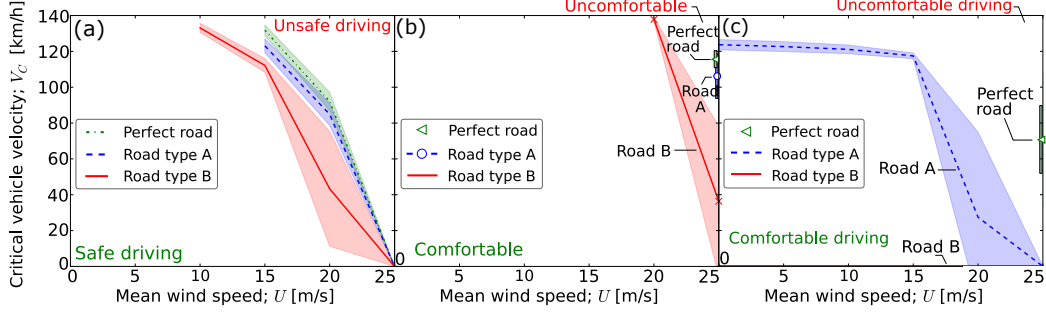
Figure 13: CWC for different road qualities: (a) global vehicle accident risk, (b) discomfort risk at the vehicle centroid, (c) discomfort risk at the vehicle cabin. $N_{r,\mathrm{ref}} = 20$.

(road type A) the ride is uncomfortable in the cabin of the truck above approximately $V = 120$ km/h, even without wind, and road type B induces discomfort for any wind and driving speed combination. Without loss of generality in the previous discussion, it should be mentioned that the CWC were obtained ignoring the actual wind shielding of the Queensferry Bridge, which is likely to reduce the driving accident and discomfort risks in this particular structure.

5.2. Transverse correlation in the pavement irregularities

The risks of accidents and discomfort with different types of correlation between the pavement profiles at the two wheel lines are compared for $U = 20$ m/s in Fig. 14. The first and the second rows in this figure refer to the results with road types A and B, respectively. The 'isotropic' correlation between profiles corresponds to the one given by Eqs. (2) and (3). The fully correlated and the uncorrelated road profiles (referred to as 'Full correlation' and 'No correlation' in Fig. 14, respectively) were obtained by considering the same profiles at the leeward wheels (r_L, the reference profile) as in the isotropic transverse irregularity correlations considered so far. This is done in order to minimise the influence of the record-to-record variability when comparing the results with different types of road correlations, which only change their irregularity profiles at the windward wheels (r_W). In the fully correlated irregularity surface the two parallel profiles at the vehicle wheels are identical ($r_W = r_L$) at any point along the deck, whereas in the road with no transverse correlation a completely independent set of 1D profiles was generated using Eq. (2) and applied at the windward wheels.

Fig. 14 shows that the transverse correlation between road profiles affects significantly the stability and the comfort in the vehicle, and it increases with the amplitude of the pavement irregularities. The risk of vehicle overturning is affected by the transverse road correlation, particularly in the intermediate range of vehicle driving speeds from 80 to 110 km/h, as it is depicted in Figs. 14 (a) and (d). The fully uncorrelated profiles magnify the vehicle rolling motion in this range of speeds and this results in a higher overturning risk. At the other end, if the two wheel lines are affected by fully correlated (identical) pavement profiles the road-induced vehicle roll is suppressed, which results in an overturning risk that is up to 24% and 67% smaller than in the uncorrelated case for roads A and B, respectively. The proposed isotropic correlation of the road irregularities lead to overturning risks that fall between the two previous extreme cases. Unlike the vehicle overturning, the side-slip is dominated by the side wind force acting on the vehicle and not by the rolling motion, which explains why the transverse correlation of the road does not influence significantly the risk of this type of accident (the differences are typically below one standard deviation of the results).

In terms of the vehicle comfort the type of transverse irregularity correlation affects significantly the truck vibrations, but only at the cabin. It is also observed that the previous trends are inverted; the more correlated the two road profiles are the more discomfort at the cabin (Figs. 14 (b) and (e)). The results show that at the vehicle driving speed for which the pitch motion resonates ($V = 70$ km/h) the driving discomfort with fully correlated road type A profiles is 24% larger than with completely uncorrelated profiles, and that difference increases up to 33% in the road with the worst quality (road type B). This is attributed to the fact that the fully correlated road surface reduces the vehicle roll and it allows a neater pitching motion, which originates the vibration problems at the cabin, as it was previously discussed.

The discomfort felt by pedestrians on the deck is not significantly influenced by the road irregularity, regardless of their transverse correlation and even of their amplitude, as shown in Figs. 14 (c) and (f).

5.3. Wheel filtering effects: disk model

It is recognised that the wheels of the vehicles have certain dimensions and they are not simply the moving points considered in *Stage 2* of the analysis. The wheel dimensions have the effect of filtering the road irregularity as it is illustrated in Fig. 1(a). This section compares the results obtained with the unfiltered profiles (i.e. with purely point wheel-pavement contacts) and
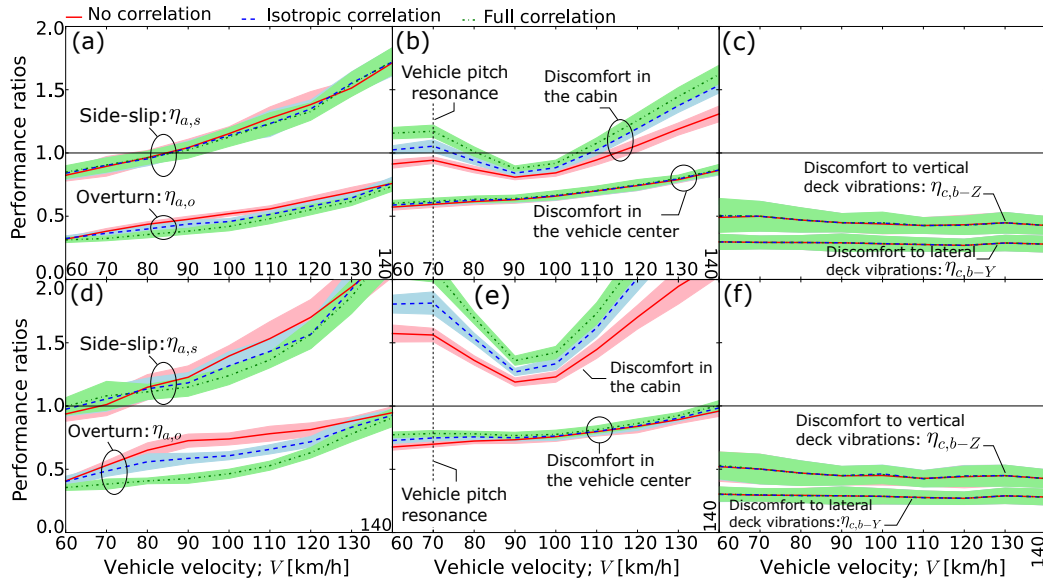
Figure 14: Peak performance risk ratios for all the vehicle velocities and different transverse correlations in the pavement profiles of the two wheel lines: (a,d) vehicle accident risk, (b,e) vehicle discomfort risk, (c,f) pedestrians' discomfort risk in storm conditions. Plots (a,b,c) correspond to Road type A, (d,e,f) refer to Road type B. $U = 20$ m/s; $N_{r,\text{ref}} = 20$.

those obtained by filtering the pavement irregularity with the 'disk model' in *Stage 1* of the proposed W-VBI framework. This model assumes that there is a single contact point between the tyre and the pavement (Point P in Fig. 1(a)) to obtain the filtered profile [8]:

$$\bar{r}_i(x) = r_i(x_P) + \sqrt{R_W^2 + d^2}, \tag{21}$$

where $\bar{r}_i$ is the filtered profile in the leeward or in the windward wheel lines ($i = L, W$, respectively); x_P is the longitudinal position of the wheel contact point P; R_W is the wheel radius; and $d = x_P - x$ is the longitudinal distance between the contact point and the center of the corresponding wheel (note that $d = 0$ if $R_W = 0$ and it leads to no filtering, which is the case considered in the previous sections). A detail of the effect of the tyre filtering in the road type B surface at one of the bridge joints with $R_W = 0.3$ m is presented in Fig. 4(b).

The complex tyre-pavement contact is simplified by considering a rigid tread band in the disk model. This type of assumption yields vehicle dynamic responses that are similar to those obtained with more refined contact models that include the tyre flexibility [34]. It should be also noted that, even though the disk model assumes rigid tyres when filtering the pavement roughness, the flexibility and the damping of the vehicle wheels is included in the *Stage 2* of the W-VBI analysis by means of springs and dashpots that connect the wheel masses with the contact points (see Fig. 1(b)).

Fig. 15 presents the influence of the wheel irregularity filtering for $U = 20$ m/s and $R_W = 0.3$ m. The disk model does not have a significant influence on the vehicle stability (see Figs. 15(a) and (d)). However, it reduces slightly the vehicle discomfort risk in the cabin regardless of the driving velocity because the magnitude of the irregularities affecting the wheels is decreased (i.e. $|\bar{r}| \leq |r|$). Figs. 15(b) and (e) suggest that the filtering effect is more appreciable in road type B, but in both pavements the reduction of the cabin vibrations with the disk model is approximately 5%. Finally, the wheel irregularity filtering has no influence on the pedestrian's comfort (see Figs. 15(c) and (f)).

Peak performance risk ratios for all the vehicle velocities and different transverse correlations in the pavement profiles of the two wheel lines: .
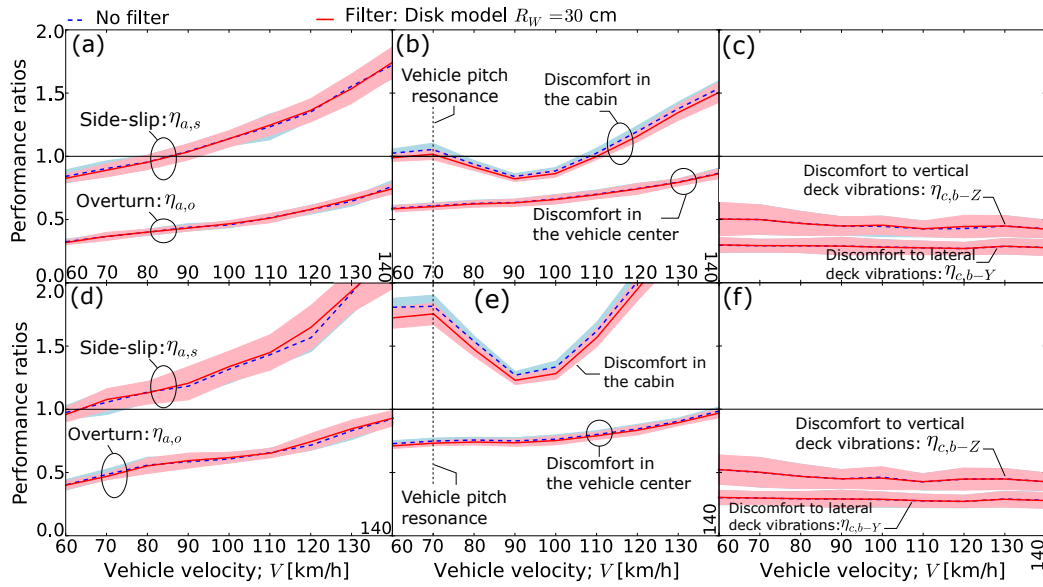
Figure 15: Influence of the wheel filtering on the peak performance risk ratios for all the vehicle velocities: (a,d) vehicle accident risk, (b,e) vehicle discomfort risk, (c,f) pedestrians' discomfort risk in storm conditions. Plots (a,b,c) correspond to Road type A, (d,e,f) refer to Road type B. $U = 20$ m/s; $N_{r,\text{ref}} = 20$

6. Conclusions

A complete wind-vehicle-bridge interaction (W-VBI) framework is presented in this work. In this methodology, the pavement irregularities are simulated as random surfaces instead of adopting the one-dimensional road generation that is traditionally used in previous W-VBI works. In addition, the bridge joints and the filtering effects of the vehicle wheels are included in the pre-processing stage of the framework. After the dynamic analysis is completed, a unified approach to assess the accident and the comfort of all users of the bridge, including those in the vehicles and on the deck, is proposed by means of performance ratios (η) and Critical Wind Curves that include the effect of the record-to-record variability.

The proposed W-VBI framework is applied to a long cable-stayed bridge to explore the influence of the wind and the pavement-induced vibrations on the driving stability and the comfort. An extensive analysis was conducted for an increasing number of wind and road irregularity records under a wide range of wind and driving speeds. It was observed that the combination of wind gusts on the vehicles and downward pavement irregularities at their wheels reduces significantly the driving stability. The results of this work demonstrate that W-VBI studies should not be based on the analysis of a single record, and it is proposed to consider 10 of them to obtain an average result with 95%-confidence in terms of the vehicle accident risk. The vehicle comfort is less sensitive to the randomness of the wind and the pavement; the results indicate that 4 records are sufficient to get a meaningful average. It is also observed that the vibrations at the cabin are significantly affected by the road-induced pitching motion, which is maximised for certain driving speeds. A significant number of different records (100 or more) needs to be considered to assess the pedestrians' comfort in the entire length of the deck.

It was concluded that in a long-span bridge the response of the deck is mainly affected by the direct wind actions and not by the vehicle-induced vibrations. On the other hand, the vehicles are mostly influenced by the wind and by the pavement irregularities. The amplitude of these irregularities directly increases the vehicle accident and discomfort risks, particularly for high wind speeds. Consequently, appropriate inspection programmes should be designed by the bridge operator to keep the pavement at the highest possible quality. The effect of the transverse correlation between the road profiles at the vehicle wheel lines is also important in terms of the overturning stability and the comfort of the vehicles. Assuming completely correlated pro-

files significantly underpredicts the overturning accident risk and maximises the vehicle discomfort at the cabin. Considering completely uncorrelated pavement records have the opposite effect. The proposed framework models the surface of the pavement irregularities by considering that the statistical properties of the road are the same in any direction (isotropy), which yields vehicle responses that are between those obtained with fully correlated and uncorrelated profiles.

Finally, the road profiles were filtered to account for the effect of the vehicle wheel dimensions. It is observed that, for a typical wheel radius and for the pavement irregularity amplitudes that are conventional in important road bridges, the filtering effects are not relevant in terms of the bridge response and of the vehicle driving safety. This type of pavement filtering is only necessary if the vehicle users' comfort needs to be accurately assessed.

Appendix A

Table 2 includes the mechanical properties of the vehicles considered in this work.

Parameter	Units	Value
Full length of the vehicle	m	13.45
Longitudinal distance from the centroid to the front wheels	m	3
Longitudinal distance from the centroid to the to rear wheels	m	5
Reference area (A_v)	m^2	10.5
Vertical distance between wheels and centroid	m	1.5
Half distance between wheel lines (b)	m	1.1
Vertical distance between upper suspension and centroid	m	0.8
Mass of the vehicle body	kg	4480
Pitching moment of inertia of vehicle body	kg·m^2	5516
Rolling moment of inertia of vehicle body	kg·m^2	1349
Mass of each wheel in front axle	kg	800
Mass of each wheel in rear axle	kg	710
Upper vertical spring stiffness (all wheels)	kN/m	399
Upper lateral spring stiffness (all wheels)	kN/m	299
Upper vertical damper damping coefficient in front wheels	kN·s/m	23.21
Upper lateral damper damping coefficient in front wheels	kN·s/m	23.21
Upper vertical damper damping coefficient in rear wheels	kN·s/m	5.18
Upper lateral damper damping coefficient in rear wheels	kN·s/m	5.18
Lower vertical spring stiffness (all wheels)	kN/m	351
Lower lateral spring stiffness (all wheels)	kN/m	121
Lower vertical damper damping coefficient (all wheels)	kN·s/m	0.8
Lower lateral damper damping coefficient (all wheels)	kN·s/m	0.8

Table 2: Mechanical properties of the vehicles considered in this study. Taken from [2].

References

[1] C. Cai, S. Chen, Framework of vehicle-bridge-wind dynamic analysis, Journal of Wind Engineering and Industrial Aerodynamics 92 (2004) 579–607.

[2] Y. Xu, W. Guo, Dynamic analysis of coupled road vehicle and cable-stayed bridge systems under turbulent wind, Engineering Structures 25 (2003) 473–486.

[3] S. Chen, C. Cai, Accident assessment of vehicles on long-span bridges in windy environments, Journal of Wind Engineering and Industrial Aerodynamics 92 (2004) 991–1024.

[4] Y. Xu, W. Guo, Effects of bridge motion and crosswind on ride comfort of road vehicles, Journal of Wind Engineering and Industrial Aerodynamics 92 (2004) 641–662.

[5] I. Kavrakov, A. Camara, G. Morgenthal, Influence of aerodynamic model assumptions on the wind-vehicle-bridge interaction, in: IABSE Symposium, Stockholm, 2016, pp. 1152–1159.

[6] K. Nguyen, A. Camara, O. Rio, L. Sparowitz, Dynamic effects of turbulent crosswind on the serviceability state of vibrations of a slender arch bridge including wind-vehicle-bridge interaction, Journal of Bridge Engineering 22 (11) (2017) 6017005–6017005.

[7] W. Guo, Y. Xu, Safety analysis of moving road vehicles on a long bridge under crosswind, Journal of Engineering Mechanics 132 (4) (2006) 438–446.

[8] A. Camara, K. Nguyen, A. Ruiz-Teran, P. Stafford, Serviceability limit state of vibrations in under-deck cable-stayed bridges accounting for vehicle-structure interaction, Engineering Structures 61 (2014) 61 – 72.

[9] A. Camara, A. Ruiz-Teran, Multi-mode traffic-induced vibrations in composite ladder-deck bridges under heavy moving vehicles, Journal of Sound and Vibration 355 (2015) 264–283.

[10] ISO 8608:1995: Mechanical vibration - Road surface profiles - Reporting of measured data (1995).

[11] A. Camara, V. Vazquez, A. Ruiz-Teran, S. Paje, Influence of the pavement surface on the vibrations induced by heavy traffic in road bridges, Canadian Journal of Civil Engineering 12 (44) (2017) 1099–1111.

[12] J. Oliva, J. Goicolea, P. Antolin, M. Astiz, Relevance of a complete road surface description in vehicle-bridge interaction dynamics, Engineering Structures 56 (2013) 466–476.

[13] Y. Han, C. Cai, J. Zhang, S. Chen, X. He, Effects of aerodynamic parameters on the dynamic responses of road vehicles and bridges under crosswinds, Journal of Wind Engineering and Industrial Aerodynamics 134 (2014) 78–95.

[14] Y. Zhou, S. Chen, Fully coupled driving safety analysis of moving traffic on long-span bridges subjected to crosswind, Journal of Wind Engineering and Industrial Aerodynamics 143 (2015) 1–18.

[15] Q. Ding, L. Zhu, H. Xiang, An efficient ergodic simulation of multivariate stochastic processes with spectral representation, Probabilistic Engineering Mechanics 26 (2011) 350–356.

[16] C. Dodds, J. Robson, The description of road surface roughness, Journal of Sound and Vibration 31 (2) (1973) 175–183.

[17] M. Sayers, Dynamic terrain inputs to predict structural integrity of ground vehicles, Tech. rep., University of Michigan / Transportation Research Institute (Rep. No. UMTRI-88-16), Ann Arbor,MI, organizational Results Research Report (0R08.003) (1988).

[18] X. Chen, A. Kareem, Advances in modeling of aerodynamic forces on bridge decks, Journal of Engineering Mechanics 176 (2018) 825–839.

[19] I. Kavrakov, G. Morgenthal, A comparative assessment of aerodynamic models for buffeting and flutter of long-span bridges, Engineerng 3 (2017) 823–838.

[20] R. Scanlan, Motion-related body-force functions in two-dimensional low-speed flow, Journal of Fluids and Structures 14 (2000) 49–63.

[21] L. Caracoglia, N. Jones, Time domain vs. frequency domain characterization of aeroelastic forces for bridge deck sections, Journal of Wind Engineering and Industrial Aerodynamics 91 (2003) 371–402.

[22] A. Davenport, The response of slender, line-like structures to a gusty wind, Proceedings of the Institution of Civil Engineers 23 (3) (1962) 389–408.

[23] R. Scanlan, The action of flexible bridges under wind, I: flutter theory, Proceedings of the Institution of Civil Engineers 60 (2) (1978) 187–199.

[24] I. Kavrakov, G. Morgenthal, A synergistic study of a CFD and semi-analytical models for aeroelastic analysis of bridges in turbulent wind conditions, Journal of Fluids and Structures 82 (2018) 59–85.

[25] I. Kavrakov, G. Morgenthal, Aeroelastic analyses of bridges using a pseudo-3D vortex method and velocity-based synthetic turbulence generation, Engineering Structures 176 (2018) 825–839.

[26] A. Irwin, Human response to dynamic motion of structures, The Structural Engineer 56A (9) (1978) 237–244.

[27] ISO 2631:1997: Mechanical vibration and shock – Evaluation of human exposure to whole-body vibration Part 1: General requirements (1997).

[28] ABAQUS, Version 6.13-3. commercial finite element software, Providence (USA) (2013).

[29] EN1991-2, Eurocode 1: Actions on structures - part 2: Traffic loads on bridges, eN 1991-2:2003 (2003).

[30] G. Solari, G. Piccardo, Probabilistic 3-d turbulence modeling for gust buffeting of structures, Probabilistic Engineering Mechanics 16 (2001) 73–86.

[31] G. Morgenthal, Aerodynamic analysis of structures using high-resolution vortex particle methods, Ph.D. thesis, University of Cambridge. (2002).

[32] G. Morgenthal, J. Walther, An immersed interface method for the vortexin-cell algorithm, Computers and Structures 85 (2007) 712–726.

[33] B. Efron, R. Tibshirani, An Introduction to the Bootstrap, Chapman & Hall/CRC, New York (USA), 1993.

[34] K. Captain, A. Boghani, D. Wormley, Analytical tire models for dynamic vehicle simulation, Vehicle System Dynamics 8 (1979) 1–32.